# Passive Elbow Joint Impedance Identification with the use of an Elbow Device

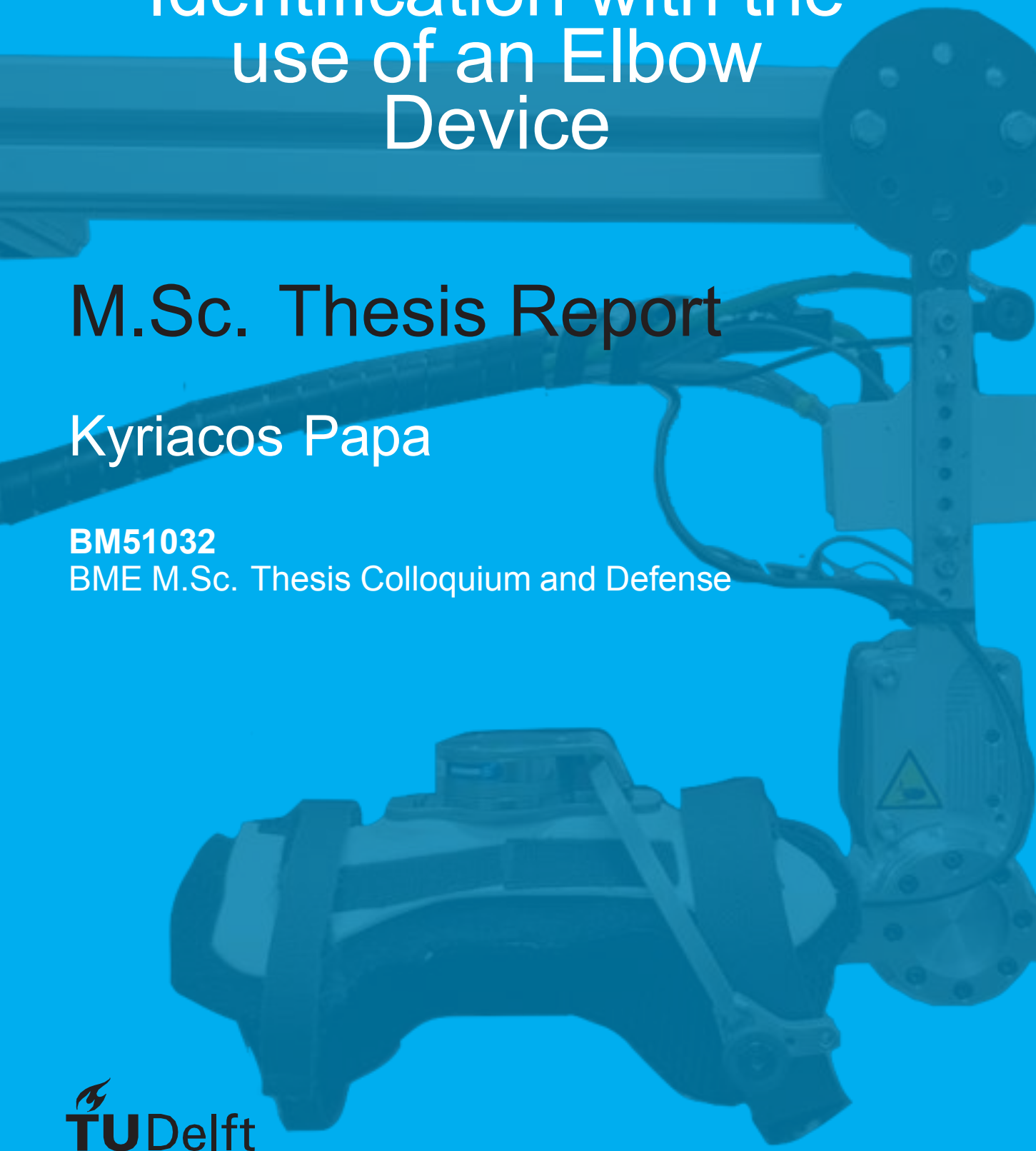

## M.Sc. Thesis Report

Kyriacos Papa

**BM51032**
BME M.Sc. Thesis Colloquium and Defense

TU Delft

# Passive Elbow Joint Impedance Identification with the use of an Elbow Device

## M.Sc. Thesis Report

by

Kyriacos Papa

to obtain the degree of Master of Science in BioMedical Engineering at the Delft University of Technology,
to be defended publicly on Tuesday August 22, 2023 at 13:30 PM.

| | |
|---|---|
| Thesis committee: | Prof. dr. ir. J. Harlaar,<br>Drs. ir. S. Filius,<br>Dr. Ir. G. Radaelli, |
| Student number: | 4922999 |
| Place: | Faculty of Mechanical, Maritime and Materials Engineering (3ME) |
| Project duration: | June 1, 2021 – August 22, 2023 |



TU Delft

TUDelft

# Passive Elbow Joint Impedance Identification with the use of an Elbow Device

Kyriacos Papa (M.Sc. Student - 4922999), drs.ir Suzanne Filius (Supervisor) and Prof.dr.ir Jaap Harlaar (Supervisor)

*Department of Biomechanical Engineering, Delft University of Technology, Postbus 5, Delft, 2600 AA, The Netherlands*
*This document was submitted on the 13th of August 2023 for the completion of the course BM51032 - BME M.Sc. Thesis Colloquium and Defense.*

ARTICLE INFO

*Keywords*:
Stiffness
Passive Joint Impedance
Elastic Property
Elastic Response
Hysteresis
Elbow Joint
Upper Extremities
Duchenne
Becker
Muscular Dystrophy
Neuromuscular Diseases
Assistive Devices

ABSTRACT

Neuromuscular diseases often result in elevated passive joint impedance (PJI), impacting the daily lives of affected individuals. To be able to apply assistive devices that compensate for PJI, it is essential to identify the PJI correctly. This study aims to identify and model the PJI of the elbow joint, to improve the control of force-based controlled active-assistance exoskeleton devices by distinguishing the voluntary from the passive forces. We used an elbow device to measure the PJI in twelve healthy males with the shoulder abducted at a 90° angle. The study investigates both static and dynamic conditions, encompassing various contraction velocities ($\leq 0.20\,\mathrm{rad/s}$) and shoulder flexion positions (0° and ±45°). The analysis estimates the hysteresis, equilibrium position, and elastic property. Subsequently, based on the average elbow PJI, we developed a regression model, with the statistical analysis revealing no significant differences between the conditions, except for the observed hysteresis under varying velocities. Based on the tested conditions, the findings indicate that a single low-velocity dynamic measurement can serve as the basis for deriving a general elbow PJI regression model.

## 1. Introduction

Duchenne muscular dystrophy (DMD) is the most prevalent muscular condition in boys, affecting newborns with an incidence rate of approximately 1 in 5000 (Mendell and Lloyd-Puryear, 2013). DMD arises from a mutation in the X-chromosome dystrophin gene, causing morphological changes to the muscles, permanently degrading them and replacing muscle fibres with adipose (i.e. fat) and connective tissue (i.e. fibrosis) (McDonald et al., 1995; Wang et al., 1999; Cornu et al., 2001; Janssen et al., 2017). These changes lead to muscle weakness and increased passive joint impedance (PJI) (Lobo-Prat et al., 2017), resulting in significant joint range of motion (RoM) reduction, loss of ambulation and upper extremity function loss (Brooke et al., 1989; McDonald et al., 1995; Wang et al., 1999; Cornu et al., 2001; Ragonesi et al., 2012; Maggioni et al., 2016; Straathof et al., 2016; Demir et al., 2020), which increase their dependency on family members and caretakers for their daily activities (Zhang et al., 2009; Lobo-Prat et al., 2017). While no cure exists, medical treatments and interventions have increased life expectancy, with progressive limb function loss further hindering their independence and, eventually, social participation (Pandya et al., 1985; Janssen et al., 2014; Mayhew et al., 2020).

To enhance independence and social engagement for individuals with DMD, passive-assistive devices like the passive version of the Wilmington Robotic Exoskeleton (WREX) (JAECO Orthopedic, Hot Springs, AR) can compensate for the arm's weight (Ragonesi et al., 2011, 2012). However, as the disease progresses and arm functionality further declines, these passive devices become insufficient, unable to facilitate arm elevation nor support additional weights (Ragonesi et al., 2011; Lobo-Prat et al., 2015, 2016, 2017). Attempting to address these limitations led to the development of active-assistive devices, which actively compensate for PJI and the arm's weight. Studies by Lobo-Prat et al. (2015, 2017); Straathof et al. (2016) demonstrated that impedance compensation using the active A-Arm (Flextension Project, The Netherlands) planar support system and the UR5 Robotic arm (Universal Robots, Denmark) increased functional RoM for users with DMD.

One of the methods employed to control these devices is force-based control which requires precise identification of the user's intention (Ragonesi et al., 2012; Lobo-Prat et al., 2015, 2017). Force sensors measure gravitational load, PJI, voluntary forces from the user, and forces resulting from involuntary muscle activation (Ragonesi et al., 2012; Lobo-Prat et al., 2015; van den Noort et al., 2017). However, individuals with muscle weakness exhibit a substantial

**Table 1**
Subject characteristics.

| Subject | 1 | 2 | 3 | 4 | 5 | 6 | 7 | 8 | 9 | 10 | 11 | 12 | mean (±SD) |
|---|---|---|---|---|---|---|---|---|---|---|---|---|---|
| Age (yr) | 28 | 32 | 25 | 35 | 24 | 28 | 30 | 25 | 24 | 30 | 34 | 33 | 29 (±4) |
| Height (cm) | 170 | 185 | 186 | 184 | 188 | 169 | 176 | 196 | 194 | 177 | 164 | 167 | 179.7 (±10.7) |
| Mass (kg) | 77 | 73 | 102 | 84 | 61 | 68 | 61 | 98 | 85 | 78 | 68 | 58 | 76.1 (±14.2) |

gravitational to voluntary-force ratio (Ragonesi et al., 2012), making the distinction between voluntary forces and other measured forces essential for accurately ascertaining the user's intention (Ragonesi et al., 2012; Lobo-Prat et al., 2015). Without monitoring electromyographic (EMG) activity, neural from non-neural contributions cannot be distinguished, so the total perceived resistance cannot be separated into purely passive or contaminated by muscle activity due to stretch reflex or involuntary background activation (van den Noort et al., 2017). Accurately identifying the elbow PJI and effectively differentiating it from the arm's weight and other neural contributions can significantly enhance the force-based control of active assistive devices (Ragonesi et al., 2012; Lobo-Prat et al., 2015).

Achieving an objective and repeatable quantification of PJI requires using instruments, such as robotic devices (Roberson and Giurintano, 1995; Cornu et al., 2001; Maggioni et al., 2016; van den Noort et al., 2017; Janssen et al., 2017). Various studies have employed such systems, recording the torque-angle relationship during different types of torque or position perturbations and measuring changes in position or torque (Boon et al., 1973; Dai et al., 2013; Maggioni et al., 2016). Perturbation methods include, among others, static measurements (Gialias and Matsuoka, 2006; Deshpande et al., 2011; Ragonesi et al., 2012), ramp-type movements (Pisano et al., 1996; Sepehri et al., 2007; Klomp et al., 2013, 2018; Kuxhaus et al., 2014; Lobo-Prat et al., 2015, 2016; Straathof et al., 2016), and frequency perturbations (MacKay et al., 1986; Zhang et al., 2000; Zhang and Rymer, 2001; Cornu et al., 2001). Unlike frequency perturbations, ramp-type movements are not limited to a small RoM where the system is considered linear and can be applied over a broad range of velocities, making them more suitable for modelling the PJI of neuromuscular diseases (Wiegner and Watts, 1986; Pisano et al., 1996; Kuxhaus et al., 2014; Ragonesi et al., 2012; Straathof et al., 2016; Lobo-Prat et al., 2016, 2017). For DMD in particular, most studies identified in the literature utilised ramp movements over the elbow's or arm's horizontal RoM with a low velocity (e.g. 0.05 rad/s), which allowed them to estimate both gravity and PJI forces (Straathof et al., 2016; Lobo-Prat et al., 2015, 2016, 2017).

Different parameters can affect the elbow PJI, and when trying to model it, it is essential to know which ones affect it and to what degree. Joint position (Deshpande et al., 2011; Landin and Thompson, 2011), including the effect of biarticular muscle (Winters and Kleweno, 1993; Zhang et al., 2009; Deshpande et al., 2011; Landin and Thompson, 2011; Günzkofer et al., 2011), and contraction velocity (Boon et al., 1973; Zhang et al., 2000, 2009; Wu et al., 2018), determine the PJI of the full RoM, and their investigation could provide a "baseline" PJI behaviour before introducing the effects of other parameters, like short-range stiffness (MacKay et al., 1986; de Vlugt et al., 2011; Drake and Charles, 2014; Pando et al., 2014) or temperature and thixotropy changes (Lakie et al., 1986; Sekihara et al., 2007).

This study's primary objective is to measure and model the elbow PJI to enhance the control of active-assistive devices. Specifically, we investigate the influence of different movement velocities and shoulder flexion positions (SFP) on elbow PJI. The application of this research could be expanded to other neuromuscular diseases requiring active support.

## 2. Methods

### 2.1. Subject Recruiting

The Human Research Ethics Committee of the Delft University of Technology approved the study on June 10th, 2022 (ID2284). After giving their informed consent, 12 healthy adult males with ages ranging from 24 to 35 years old participated in the study. All the participants were healthy with no prior injuries or dislocation to their upper extremities. Table 1 summarises the subjects' main characteristics.

### 2.2. Setup: Prototype Elbow Device

The elbow device is a one-degree-of-freedom (DOF) prototype system (see Fig. 1) designed to investigate the elbow PJI. In addition to the active 1-DOF, which is aligned to the user's elbow joint, the device attaches to an aluminium frame allowing for two additional manual shoulder DOF (shoulder flexion in steps of 22.5° and continuous shoulder

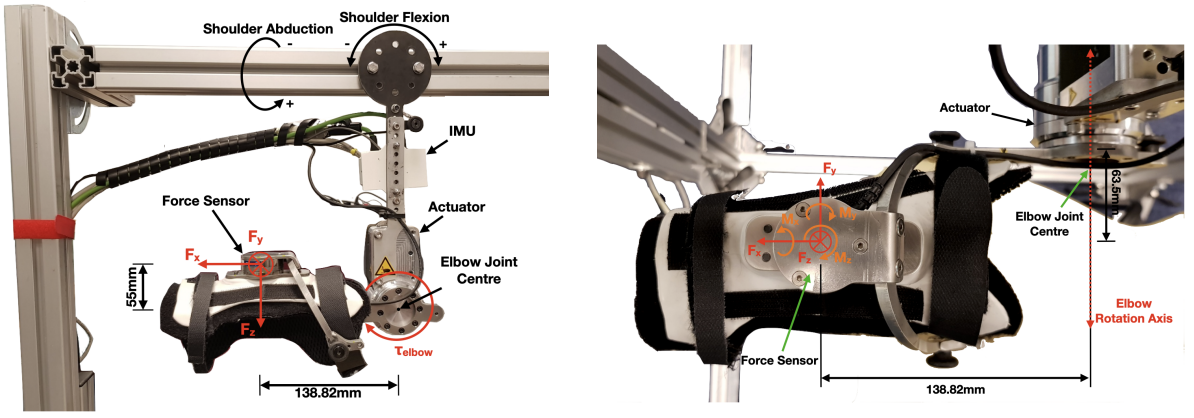


**(a)** Side view of the setup.

**(b)** Close-up top view of the setup.

**Figure 1:** Setup side and top view showing the force/torque sensor coordinate system and different parts of the setup.

abduction of 0 to 90°). For safety purposes, the setup possesses both mechanical and software RoM end-stops. A metallic beam extends from the actuator and runs down the forearm axis, with a sleeve attached at its end. The sleeve is made out of thermoplastic material and is lined with padding. Located between the sleeve and the forearm lever, a 6-DOF strain-gauge-based force/torque (FT) sensor FT-Mini-40 SI-80-4 (Schunk GmbH & Co. KG, Germany) measures the interaction forces and torques between the user and the device. The FT sensor and actuator data are all recorded by a base station (Beckhoff C 6025 0020 IPC) after passing through an analogue-to-digital converter, where they are sampled at 1 kHz and a resolution of 16 bits. The measurement error is less than ±0.3 % relative to the full scale of 10 V ($\epsilon_{F_{x,y}} = \pm 0.24\,\text{N}$, $\epsilon_{F_z} = \pm 0.72\,\text{N}$, $\epsilon_{M_{x,y,z}} = \pm 0.012\,\text{Nm}$). Before each session, we calibrated the FT sensor, correcting any offset (see Appendix Section A.3.1). We filtered all the FT sensor data with a 2nd-order Low-Pass Butterworth filter with a cut-off frequency of 10Hz. The FT sensor coordinate system is expressed at the setup's elbow joint centre (EJC) to measure the elbow joint torque (EJT) (see Fig. 1). For more information on the process, refer to Appendix section A.6. We validated the EJT reading against a provided gravity model, giving a root-mean-square (RMS) accuracy of smaller than 0.1 Nm (see Appendix Section A.7). A Simulink model (Matlab version 2019b (The MathWorks Inc, Massachusetts, USA)) (stored in a private repository) running on TwinCAT 3 (Beckhoff Automation, Verl, Germany) and remotely configured through a second computer (ThinkPad P15s Gen 1, Lenovo Group Limited, Beijing, China) controls the actuator.

The subjects were seated in a chair with a cushion behind their back for comfort and to maintain an upright position during the trials. The setup height and upper arm lever length were adjusted to accommodate the subjects' height and upper arm length differences to align the actuator with the subject's EJC (MacKay et al., 1986). The EJC, defined as the lateral epicondyle of the elbow joint, was carefully aligned to the actuator's centre of rotation to avoid any measurement inaccuracies (Maggioni et al., 2016).

## 2.3. Electromyographic recording

To ensure the exclusion of data contaminated by muscle activity (Sepehri et al., 2007), we employed the Delsys Trigno® Wireless Biofeedback System (Delsys, USA), featuring the Trigno Avanti™ sensors, to accurately monitor the electromyographic (EMG) activity of both heads of the m. Biceps Brachii (BB) and m. Triceps Brachii (TB) Long Head. The surface EMG (sEMG) electrodes were placed in the direction of the muscle fibres according to the SENIAM (Surface ElectroMyoGraphy for the Non-Invasive Assessment of Muscles) guidelines (Hermens et al., 1999). The sEMG was recorded at 1.111 kHz, and an online visual inspection of the sEMG activity during and at the end of each experiment ensured the correct data recording. The sEMG data were exported into a comma-separated value (CSV) file and then processed using Matlab version 2021a (The MathWorks Inc, Massachusetts, USA). The sEMG signals were high-pass filtered at 20 Hz using a 3rd-order Butterworth filter to remove any residual artefacts, then rectified and finally, low-pass filtered using a 2nd-order Butterworth filter at 3 Hz to obtain the smoothed rectified sEMG. To initiate and synchronise the sEMG system with the actuator setup, we employed the dedicated Delsys® Trigger

**Table 2**
Experimental conditions.

| Velocities at 0° | | | | Shoulder Flexion | | |
|---|---|---|---|---|---|---|
| Shoulder Flexion (rad/s) | | | | Positions at 0.10 rad/s | | |
| Static | 0.05 | 0.10 | 0.20 | −45° | 0° | +45° |

Module SP-U02 (Delsys, USA). To prevent interference from the actuator, we positioned an insulating piece of fabric between the shoulder joint and the shoulder plate. Subsequently, all signals were recorded and stored for offline analysis.

## 2.4. Experimental Protocol

### *2.4.1. Overview*

Each session lasted a maximum of three hours and included a series of anthropometric measurements (for more details, see subsection 2.4.2), the placement of the sEMG electrodes and followed by the recording of the trials. We asked the subjects not to consume caffeine on the day of the experimental session, and during the trials, we asked them to relax by closing their eyes, with the option of listening to relaxing music. They were also free to take breaks or withdraw from the experiments at any point during the session. We recorded the EJT with the shoulder abducted at 90°. Experimental conditions with neutral (0°) SFP included static and dynamic measurements at three constant velocities, 0.05, 0.10 and 0.20 rad/s (≈3, 6 and 12 deg/s). Additionally, we tested two different SFPs of ±45° at 0.10 rad/s. Each subject's investigated RoM was 80 % of their comfortable passive RoM (pRoM), which the examiner obtained by manually moving the subject's forearm while in the setup. First, we randomly tested the conditions of the neutral SFP, followed by the random order of the two non-neutral SFPs. The trial began from the most extended position of the elbow joint (fully extended at 0°), reached the most flexed position and finally went back to the most extended position to complete a full cycle. Table 2 provides an overview of the tested conditions, whereas Fig. 2 illustrates the tested SFPs along with a snapshot from the trials.

### *2.4.2. Anthropometric Measurements*

Before the experimental session, we measured each subject's height, weight, and segment lengths of their right arm (when in anatomical position) and estimated the volume of their hand and forearm. We measured the distance between

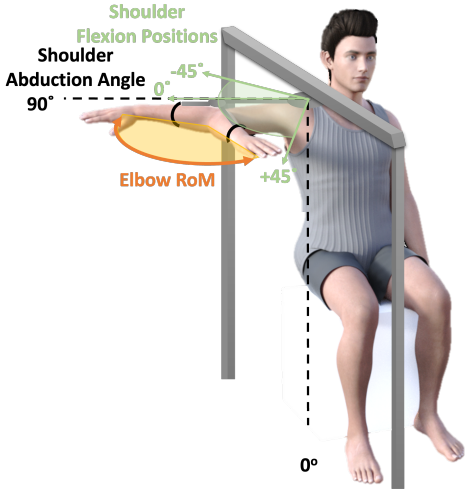


**(a)** Illustration of subject and setup with the tested elbow and shoulder RoM. Illustration by Suzanne Filius.

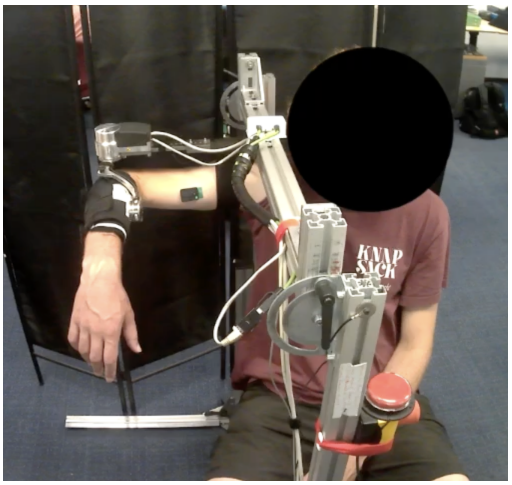

**(b)** Front-view of a subject and the setup during an experimental trial.

**Figure 2:** Setup and subject pictures displaying the experimental conditions. Fig. 2a illustrates the positions tested, with the elbow and shoulder RoM. Fig. 2b shows a snapshot taken during a trial.

the acromion, EJC (lateral epicondyle), wrist joint centre (WJC) (defined as the midpoint between the radial and ulnar styloid process) and the tip of the middle finger to determine the segment lengths of the upper arm, forearm and hand. The upper arm volume was estimated by modelling it as a cylinder with an average circumference of three equidistant points between the elbow and shoulder joints. We estimated the mass of the hand and forearm by multiplying their segment density values with the volume of the overflown water when we submerged each segment in a container. We then estimated the hand and forearm's combined centre-of-mass (COM) location from the individual segment COM locations (Dempster, 1955; Clauser et al., 1969; Plagenhoef et al., 1983; Winter, 2009).

#### *2.4.3. Static Experiments*

The static experiments involved one complete flexion/extension cycle comprising 12 equidistant positions distributed along the RoM. The actuator maintained each position for 15 s before moving to the next one at a constant velocity of 0.1 rad/s. The experiment starts from the 90° position and then moves to the first most extended plateau. There are 23 recorded plateaus, with the 12th plateau treated as the last of the flexion sequence and the first of the extension sequence.

#### *2.4.4. Dynamic Experiments*

In the dynamic conditions, the actuator moved the participant's elbow joint at a constant angular velocity, starting from the most extended position and completing eight flexion/extension cycles. We always excluded the first and final cycles from the analysis based on the assumption that the PJI may increase by anticipating the onset of the perturbation of the first cycle (Holmes et al., 2015) or by other effects such as Short-Range Stiffness (MacKay et al., 1986; de Vlugt et al., 2011; Drake and Charles, 2014). Whereas for the last cycle, subjects could anticipate when the trial would end and stop relaxing.

### 2.5. Data Analysis

#### *2.5.1. Data Structuring*

Both experiment types follow a similar processing procedure. We synchronised the corresponding sEMG signals with the actuator and FT data and separated them into plateaus (static) and cycles (dynamic). We divided the dynamic experiments into eight distinct flexion and extension cycles, whereas, in the static experiments, we identified the 6 s to 12 s window of each 15 s plateau, based on which we estimated the EJT as the average torque over the 6 s.

#### *2.5.2. Data Exclusion*

We excluded data based on sEMG activity, video feedback, and the torque-angle curves. Preliminary studies indicated that, in some cases, the sEMG activity during a fully relaxed state with no joint movement differed from the activity recorded during movement. Consequently, we determined the relaxed-state threshold by considering the muscle activity specific to each trial.

We made the assumption that during dynamic conditions, in three out of eight cycles (including the first and last cycle), the subject is relaxed, with minimal muscle activity. For each trial, we selected the three cycles with the lowest average sEMG activity, based on which we calculated a new mean sEMG level and noise (i.e. standard deviation (SD)). Finally, we calculated the threshold for each muscle by setting it at three times the noise level over the mean of the sEMG signal. We considered each contraction phase contaminated with activity and excluded them when 5 % of the contraction phase surpassed the threshold. After computing the threshold, we always excluded the first and last cycles.

Similarly, for the static conditions, we assumed a relaxed state for nine out of 23 plateaus (same ratio 3:8), based on which we calculated the same metrics (i.e. mean sEMG, noise and threshold). In this case, we excluded a plateau when its mean sEMG surpassed the threshold. For a more detailed process explanation, refer to Appendix Section B.2.

Following the EMG-based exclusion, we reviewed the EJT data alongside video feedback, based on which we removed any additional plateaus/cycles showing abnormal behaviour or movement. For the Static conditions, due to the presence of just 12 EJT values per contraction (flexion or extension) phase, if the remaining plateaus in either flexion or extension phase were less than ten, we excluded the trial. Fig. 3 presents examples of the process of both experiment types.

#### *2.5.3. Elastic Response*

We calculated the elastic response (Harlaar et al., 2000) of each trial as the net EJT ($\overline{\text{EJT}}$). For the static trials, we fitted the hysteresis curves (i.e. flexion/extension torque-angle curves) with a 3rd-order polynomial. If they consisted

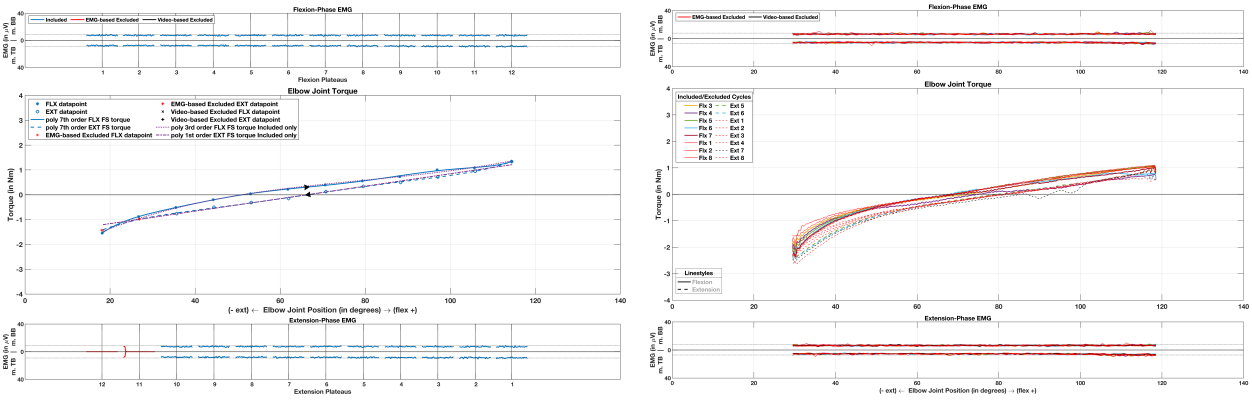


**(a)** Static trial of S09.

**(b)** Dynamic trial of S06 with a velocity of 0.10 rad/s.

**Figure 3:** Examples of static (Fig. 3a) and dynamic (Fig. 3b) trials, where the Torque Vs Angle (in Nm and degrees, respectively) curves (hysteresis loops) are displayed with their corresponding sEMG activity (in μV) (top and bottom figures) of both biceps brachii and triceps brachii muscles. The top corresponds to the flexion phase (top hysteresis curve, solid lines), whereas the bottom one corresponds to the extension phase (bottom hysteresis curve, dashed lines). The sEMG threshold for each muscle is displayed in a dotted line. The excluded plateaus/cycles based on sEMG activity appear in red. In the static case, the last two extension plateaus are excluded due to corrupted (flat) sEMG data. The flexion phase is fitted with a 3rd-order polynomial, whereas the extension phase is fitted with a regression line.

only of ten plateaus, we fitted them with a regression line (see example in Fig. 3a). We calculated the mean EJT as the average per joint angle of the two movement directions ($\overline{\text{EJT}}(\theta)_{\text{Static}} = (T(\theta)_{\text{flex}} + T(\theta)_{\text{ext}})/2$).

In the dynamic conditions, we fitted each EJT cycle with a 13th-order polynomial to smoothen out the signal and then averaged the cycles of each contraction phase. The net flexion EJT ($\overline{T}_{\text{flex}}(\theta)$) was the result of the mean of all included EJT flexion curves and similarly so was the net extension EJT ($\overline{T}_{\text{ext}}(\theta)$). Finally, the elastic response, described by the total EJT, was the resulting average per joint angle of the net flexion and extension EJT curves, $\overline{\text{EJT}}_{\text{Dynamic}}(\theta) = (\overline{T}_{\text{flex}}(\theta) + \overline{T}_{\text{ext}(\theta)})/2$ (see example in Fig. 22). In all cases, we first interpolated the torque-angle curves in the common RoM and then we averaged. For each condition (i.e. different velocities and SFPs), we obtained the mean EJT ($\overline{\text{EJT}}_{\text{cond.}}$) by averaging all the net EJT polynomials of the included trials and then fitting with a regression line. Lastly, we compared the estimated upper arm volume to the PJI obtained from the 0.10 rad/s condition at 0° SFP.

### *2.5.4. Metrics*

We calculated a series of metrics to understand better the effects of the tested velocities and SFPs on the elbow PJI. Based on the net flexion and extension EJTs, we calculate the hysteresis in two ways: (1) Hysteresis (H), which is calculated as the torque difference between flexion and extension at the mid-point of the RoM ($H(\theta) = T_{\text{flex}}(\theta) - T_{\text{ext}}(\theta)$, where $\theta = RoM/2 = (\theta_{max} - \theta_{min})/2$) and (2) total hysteresis (TH) which we calculate as the absolute area between the two curves ($TH = \int_{\theta_{min}}^{\theta_{max}} \left|\overline{T}_{\text{flex}}(\theta) - \overline{T}_{\text{ext}}(\theta)\right| d\theta$).

Due to varying RoM between subjects, we estimate the normalised hysteresis (NTH) by normalising the TH to the subject's RoM. We only estimated H and NTH under dynamic conditions because modelling some curves with a regression line under static conditions could result in inaccuracies.

Passive joint impedance also referred to as the elastic property of the joint (Sepehri et al., 2007), was estimated as the slope $\alpha$ of the regression line $y = \alpha x + b$, fitted to the net EJT (explained in subsection 2.5.3) (Pisano et al., 1996; Sepehri et al., 2007). Lastly, we identified the elbow joint equilibrium position (EP) of every trial at the zero-crossing (i.e. where the net torque is zero) of the elastic response regression line.

## 2.6. Statistics

With the use of Matlab, we examined the effects of the two factors of contraction velocity and SFPs (biarticular muscles) by performing two different one-way analyses of variance *ANOVA* tests on each one of the metrics of elastic property, equilibrium position, hysteresis, and normalised hysteresis. Performed the analysis on all the included trials (i.e. no muscle activity or movement) and used the $F$-statistic to compare the difference between group means for each factor. A significant difference was considered when $p < 0.05$.

**Table 3**
Subject anthropometric results.

| | Upper Arm | | | Forearm | | Full pRoM[e] (deg) | | 80% pRoM (deg) | |
|---|---|---|---|---|---|---|---|---|---|
| Subject | Circ.[a] (cm) | L[b] (cm) | V[c] ($\times 10^3$ cm$^3$) | COM[d] (cm) | Mass (kg) | Min[f] | Max | Min[f] | Max |
| 1 | 30.8 | 32.0 | 241.1 | 15.6 | 1.6 | 5.4 | 137.1 | 18.6 | 123.9 |
| 2 | 29.6 | 32.8 | 228.2 | 16.8 | 1.6 | 8.0 | 131.8 | 20.4 | 119.5 |
| 3 | 34.7 | 33.6 | 321.4 | 16.6 | 2.3 | 8.5 | 127.7 | 20.4 | 115.7 |
| 4 | 32.1 | 35.0 | 287.5 | 17.6 | 1.8 | 6.1 | 116.9 | 17.2 | 105.9 |
| 5 | 26.0 | 34.5 | 185.6 | 17.0 | 1.4 | 6.3 | 120.6 | 17.7 | 109.2 |
| 6 | 31.7 | 30.5 | 243.4 | 14.7 | 1.4 | 17.4 | 129.5 | 28.6 | 118.3 |
| 7 | 27.1 | 29.7 | 174.0 | 15.5 | 1.3 | 7.5 | 137.9 | 20.6 | 124.9 |
| 8 | 35.2 | 35.7 | 352.0 | 17.2 | 2.4 | 5.6 | 133.9 | 18.4 | 121.1 |
| 9 | 32.4 | 35.6 | 278.8 | 17.5 | 2.1 | 5.9 | 126.9 | 18.0 | 114.8 |
| 10 | 30.8 | 34.2 | 258.2 | 16.8 | 1.6 | 4.3 | 138.9 | 17.8 | 125.4 |
| 11 | 30.0 | 29.7 | 212.7 | 13.2 | 1.4 | 3.3 | 128.4 | 15.9 | 115.9 |
| 12 | 27.3 | 31.7 | 188.0 | 15.8 | 1.3 | 3.2 | 138.4 | 16.7 | 124.9 |
| mean | 30.6 | 32.9 | 247.6 | 16.2 | 1.7 | 6.8 | 130.7 | 19.2 | 118.3 |
| ±SD | 2.8 | 2.2 | 55.2 | 1.3 | 0.4 | 3.8 | 7.1 | 3.3 | 6.3 |

[a] Average circumference obtained from three different circumference measurements (1) elbow joint, (2) upper arm mid-point and (3) shoulder joint.
[b] Length (L) of the upper arm, measured from the acromion to the elbow lateral epicondyle.
[c] Volume (V) is approximated as a cylinder.
[d] The centre-of-mass (COM) is expressed proximal to the elbow joint.
[e] The full passive range of motion (pRoM) is the subject's comfortable RoM when in the setup.
[f] The elbow joint is fully extended at 0°.

**Table 4**
*p*-Values of *ANOVA* statistic tests.

| Condition | PJI | EP | H | NTH |
|---|---|---|---|---|
| Sh. Flex. Pos. | 0.54 | 0.33 | 0.55 | 0.25 |
| Velocity | 0.89 | 0.48 | 0.03 | 0.09 |

## 3. Results

We completed all 72 trials (12 subjects × 6 conditions), and from the exclusion process, we excluded 11 of them. Two trials were excluded as subjects S11 and S12, given their limited shoulder extension RoM, tested the −22° SFP instead of the −45°. The primary reason for excluding other trials (i.e. eight static and one dynamic trial) was elevated sEMG activity. For our analysis, we utilised the remaining trials and their included cycles. Table 9 in Appendix C shows an overview of the included trials. Also, Table 3 shows the results from every subject's anthropometric measurements.

The mean values for all four examined metrics do not exhibit significant differences between different conditions ($p > 0.09$) except for hysteresis. Hysteresis showed a significant interaction with velocities ($p = 0.03$), particularly between 0.05 rad/s and 0.20 rad/s ($p = 0.03$). For comprehensive reference, we summarise the results of the *ANOVA* tests in Table 4, the mean and SD values in Table 5, and analysis box plots are conveniently displayed in Fig. 4 and 5.

The PJI, which represents the elastic property and is derived from the slope of the torque-angle curve, exhibits no significant difference between the two factors ($p_{\text{pos.}} = 0.54$ and $p_{\text{vel.}} = 0.89$). The overall mean PJI across all conditions is $0.019 \pm 0.003$ Nm/deg. Similarly, the mean EP of all groups under either of the two factors did not show any significant difference ($p_{\text{pos.}} = 0.33$ and $p_{\text{vel.}} = 0.48$). In the case of S07 at −45° SFP, we obtained no EP since the $\overline{\text{EJT}}$ consisted of only negative values and never crossed 0 Nm (see Fig. 20 in Appendix). When positioning the shoulder joint at 90° abduction, the overall EP values have an average of $\approx 64° \pm 6°$, with the lowest EP being 32° and the highest 105°.

**Table 5**
The four metrics mean and standard deviation values (mean± SD) along with their corresponding number ($n$) of trials.

| | Velocity | | | | Shoulder Flexion Position | |
|---|---|---|---|---|---|---|
| Metrics [a] | Static ($n = 4$) | 0.05 rad/s ($n = 12$) | 0.10 rad/s ($n = 11$) | 0.20 rad/s ($n = 12$) | −45° ($n = 10$) | +45° ($n = 12$) |
| PJI (N m/rad) [b] | $1.104 \pm 0.451$ | $1.172 \pm 0.354$ | $1.120 \pm 0.391$ | $1.049 \pm 0.406$ | $1.327 \pm 0.542$ | $1.150 \pm 0.400$ |
| PJI (Nm/deg) [b] | $0.019 \pm 0.008$ | $0.020 \pm 0.006$ | $0.020 \pm 0.007$ | $0.018 \pm 0.007$ | $0.023 \pm 0.009$ | $0.020 \pm 0.007$ |
| EP (deg) [c] | $60.1 \pm 13.2$ | $62.2 \pm 12.7$ | $69.5 \pm 10.2$ | $67.5 \pm 17.2$ | $67.1 \pm 19.6$ [d] | $60.7 \pm 13.7$ |
| H (Nm) [c] | n/a | $0.5 \pm 0.2$ | $0.3 \pm 0.2$ | $0.2 \pm 0.3$ | $0.4 \pm 0.4$ | $0.3 \pm 0.2$ |
| NTH (Nm deg/deg) | n/a | $0.39 \pm 0.16$ | $0.26 \pm 0.15$ | $0.26 \pm 0.16$ | $0.39 \pm 0.22$ | $0.29 \pm 0.15$ |

[a] Metrics: Passive joint impedance (PJI), equilibrium position (EP), hysteresis (H) and normalised hysteresis (NTH).
[b] The PJI values are expressed in three decimals to match the literature formatting.
[c] Due to system accuracy, the EP and H values are rounded to one decimal.
[d] Excluding S07 since EJT was negative and failed to identify an EP.

**Table 6**
Coefficients of the linear regression model ($y = \alpha x + b$) of the elastic response of all included trials ($n$) of each condition.

| | Velocity | | | | Shoulder Flexion Position | | |
|---|---|---|---|---|---|---|---|
| Coefficient | Static ($n = 4$) | 0.05 rad/s ($n = 12$) | 0.10 rad/s ($n = 11$) | 0.20 rad/s ($n = 12$) | −45° ($n = 10$) | +45° ($n = 12$) | Mean (±SD) |
| $\alpha$ (Nm/deg) | 0.019 | 0.019 | 0.019 | 0.018 | 0.021 | 0.019 | 0.019 (±0.001) |
| b (Nm) | −1.088 | −1.196 | −1.285 | −1.109 | −1.380 | −1.109 | -1.194 (±0.117) |

Hysteresis showed a significant difference only for the velocity factor ($p_{\text{pos.}} = 0.55$ and $p_{\text{vel.}} = 0.03$), which indicates that with increasing velocity, the hysteresis declines. From 0.05 to 0.20 rad/s it reduced by 60 %. At the 0.20 rad/s condition, the hysteresis exhibits negative values as a result of overlapping flexion and extension hysteresis curves, where the flexion curve shows smaller values than the extension curve (refer to the 0.20 rad/s in the first plot of Fig. 4). The normalised hysteresis, which is obtained by normalising the area between the hysteresis curves (see Fig. 6), presents no significant difference in either of the two factors ($p_{\text{pos.}} = 0.25$ and $p_{\text{vel.}} = 0.09$). The average NTH across all conditions is $0.28 \pm 0.07$ Nm deg/deg.

The upper arm volume shows a significant correlation ($r = 0.74$, $p < 0.01$) to PJI (see Fig. 7). We fitted the data with linear regression, giving a standard error of estimate $SEE = \sqrt{\frac{\sum(y-model)^2}{n-2}} = 0.005$ Nm deg/deg. For zero PJI, this model estimates the volume of non-elastic structures of the upper arm to be approximately 384 $cm^3$.

The net elastic response (or PJI) regression model of each condition is displayed in Fig. 8, with Table 6 listing the model coefficients of each condition. The elastic property coefficient $\alpha$ (i.e. slope), has values of $0.019 \pm 0.001$ Nm/deg whereas the coefficient $b = -1.194 \pm 0.117$ Nm. Lastly, Fig. 19 in the Appendix shows an analytic comparison of each trial's elastic response regression models along with each condition's net elastic response.

## 4. Discussion

In this study, we aimed to design a method for identifying the elbow PJI, evaluate how it changes in various velocities and SFPs, and model it for compensation in force-based controlled active assistive devices. To ensure precise PJI measurements, we instructed the participants to relax completely, eliminating any torque contribution from active components, whether voluntary or involuntary. Consequently, the exclusion process removed several trials or segments contaminated with muscle activity, highlighting some subjects' difficulty achieving complete relaxation.

The *ANOVA* statistical analysis examining the effect of the velocity and SFP factors on the four metrics revealed significant difference only for the hysteresis for different contraction velocities. In particular, we observed a 60 % reduction in mean hysteresis from 0.05 rad/s to 0.20 rad/s (see the top box-plot of Fig. 4). Based on the literature, we

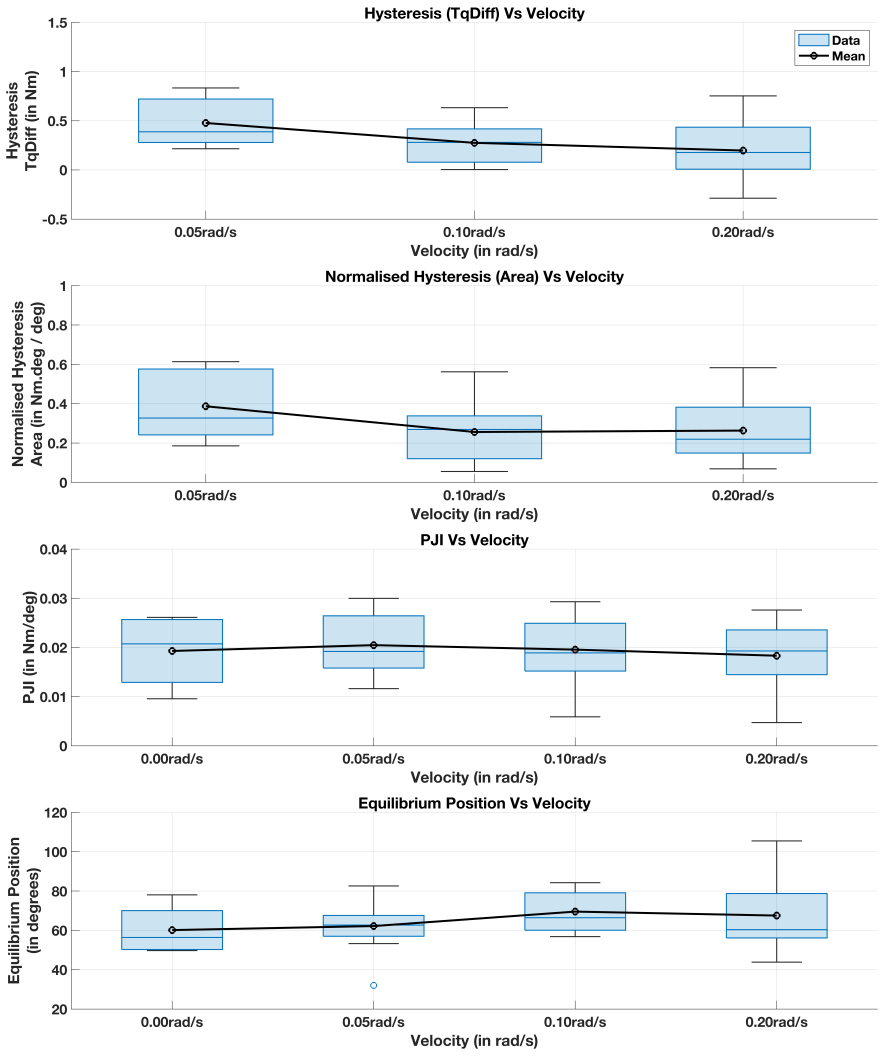


**Figure 4:** Box plots of the four metrics, elastic property or passive joint impedance (PJI), equilibrium positions, hysteresis and normalised hysteresis in relation to the velocity factor.

expect to see an increase of hysteresis with velocity (Boon et al., 1973). However, in our case, we observe the opposite. This is attributed to the negative values obtained from the calculation of hysteresis in the case of 0.20 rad/s.

In contrast, in normalised hysteresis (see 2nd box-plot of Fig. 4), where all the calculated values are positive, we see that the mean value reduces from 0.05 Nm deg/deg, but remains the same (i.e. 0.26 Nm deg/deg) for 0.10 and 0.20 rad/s. When for hysteresis we obtain only positive values as well, the mean H of 0.20 rad/s condition would also increase and potentially be higher than that of the 0.10 rad/s. These negative values are the result of the overlapping flexion and extension hysteresis curves ($\overline{T}_{flex}(\theta) < \overline{T}_{ext}(\theta)$) (see example in Fig. 9) observed in the 0.20 rad/s condition; a consequence of elevated muscle activity (see Fig. 10 and 11). This presents a limitation in our methodology when calculating the sEMG activity threshold based on each trial's sEMG activity. We made the assumption that the subjects were relaxed in three of the eight recorded cycles. Muscle activity in the three most "relaxed" cycles increases the sEMG exclusion threshold, tolerating more activity before eliminating data (see example in Fig. 11). Muscle activity is also present in the $-45°$ condition of S07 and explains why no EP was identified (see Fig. 21 in Appendix).

Moreover, with eight out of 12 trials excluded, static experiments were more prone to exclusion compared to dynamic trials. Due to time limitations, we recorded only one complete cycle per static trial, making them more susceptible to exclusion. To mitigate trial exclusion, we recommend recording more cycles for static experiments.

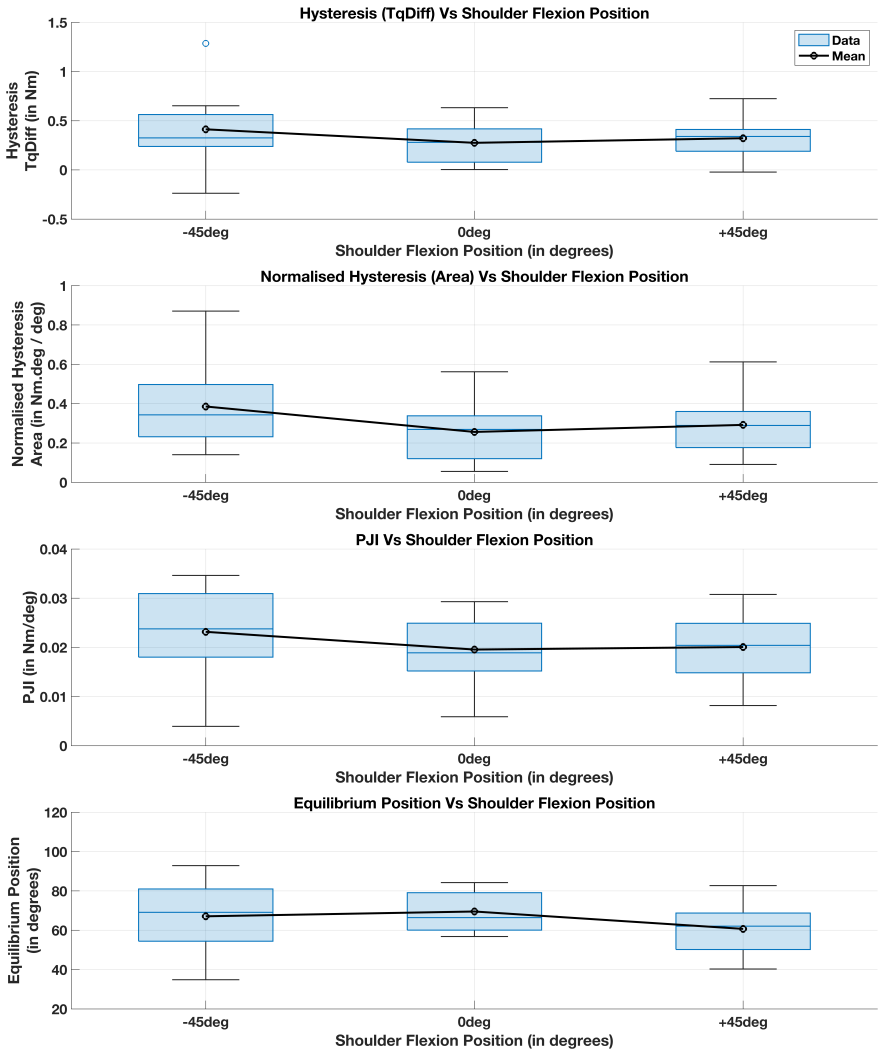


**Figure 5:** Box plots of the four metrics, elastic property or passive joint impedance (PJI), equilibrium positions, hysteresis and normalised hysteresis in relation to the shoulder flexion position factor.

Nonetheless, the *ANOVA* analysis showed no significant differences between the static condition and other velocities, allowing for the substitution of static trials with low-velocity dynamic measurements.

Considering all the conditions, the EP values have an average of approximately 65° ± 3° and range between 32° and 105°. For the same shoulder position of 0° flexion and 90° abduction, Wiegner and Watts (1986) identified the EP in the range of 107° ± 10°. Similarly, at 0° flexion and 80° abduction, Mirbagheri et al. (2006) identified the lowest PJI at 75° and Jones et al. (1987) placed it in the range of 10° to 20° when the arm is resting by the subject's body. Wu et al. (2018) defined the neutral position of the elbow joint as the place where the subjects felt the most comfortable 75° ± 6.5°, with the shoulder abducted at 75° and the wrist and forearm supported by the setup. The results are not directly comparable to the literature due to the different neutral position definition (Wiegner and Watts, 1986; Wu et al., 2018), different support (Wu et al., 2018) or due to the gravity component, which is present in the Mirbagheri et al. (2006); Jones et al. (1987) studies. However, our results are about 10° less than Mirbagheri et al. (2006); Wu et al. (2018) and differ substantially from Wiegner and Watts (1986); Jones et al. (1987).

Regarding the NTH, we estimated it at $0.28 \pm 0.07\,\mathrm{Nm\,deg/deg}$, which is substantially higher than $\approx 0.16 \pm 0.05\,\mathrm{Nm\,deg/deg}$ identified in the study of Sepehri et al. (2007). This difference could be attributed to the difference in tested velocities and RoM.

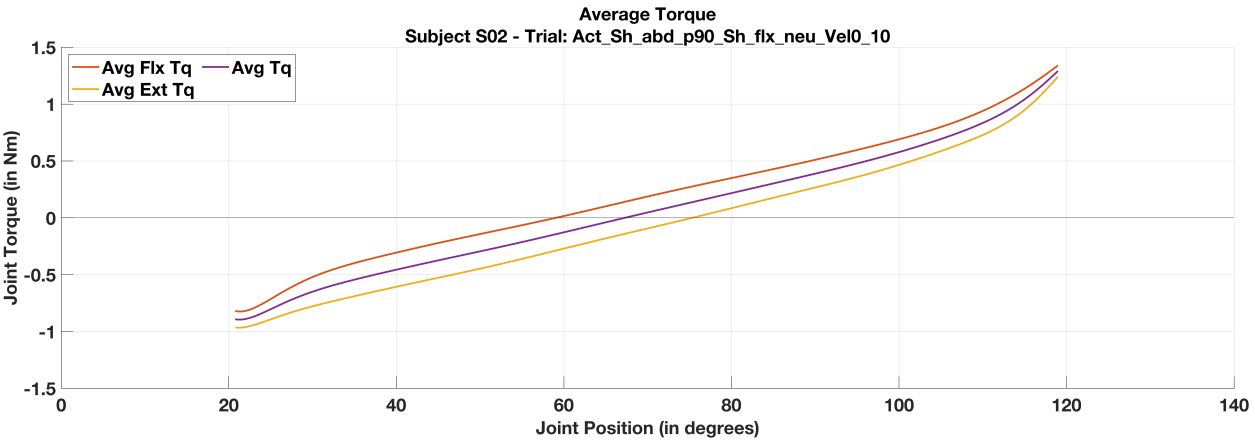


**Figure 6:** Example of a dynamic trial of S02 with 0.10 rad/s averaged flexion (top red curve) and extension (bottom yellow curve) hysteresis curves and the net elastic response (middle magenta curve).

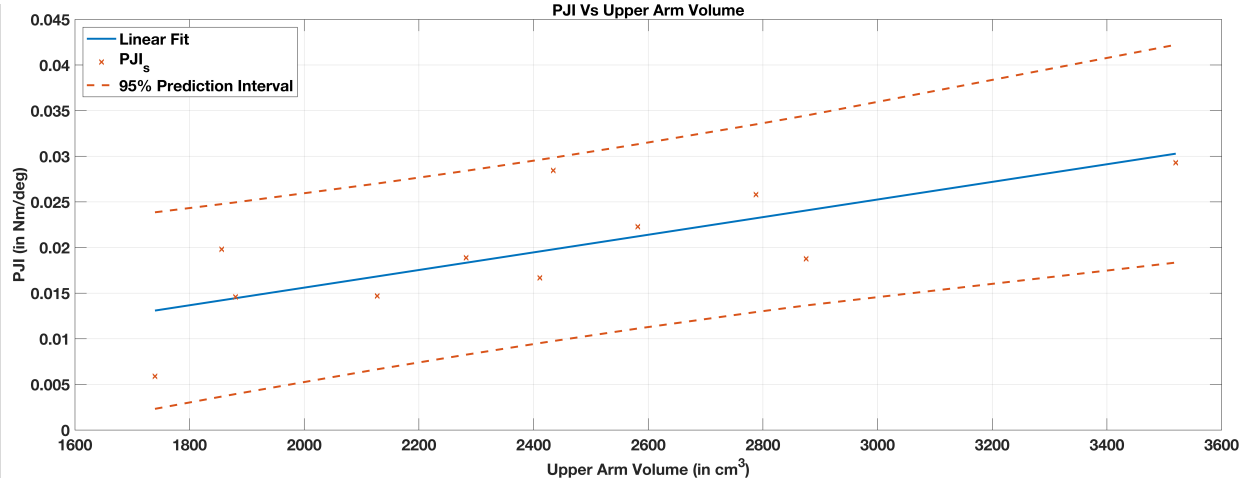


**Figure 7:** Comparing passive joint impedance (PJI) to upper arm volume.

After conducting our tests, we found that the average PJI for all conditions was $0.019 \pm 0.001$ Nm/deg. Despite some differences in research methodologies, perturbation types or arm orientation, our elbow PJI estimation agrees with the literature, $0.017 \pm 0.008$ Nm/deg (Wu et al., 2018), 0.018 to 0.08 Nm/deg (Lin et al., 2003) and $0.016 \pm 0.007$ Nm/deg (Wiegner and Watts, 1986)). Research by Sepehri et al. (2007) and Dai et al. (2013) however, resulted in higher PJI values of $0.042 \pm 0.008$ Nm/deg and $0.99 \pm 0.53$ Nm/deg, respectively. Sepehri et al. (2007) perturbed the forearm in the sagittal plane, whereas Dai et al. (2013) used much higher perturbation velocities (i.e. 30 to 240 deg/s).

Moreover, the torque-angle relationship can be considered linear around the middle of the RoM and non-linear towards the extremes (see Fig. 6). This finding is supported by Wiegner and Watts (1986), who noted a linear behaviour at $\pm 30°$ around the neutral position and exponential towards the limits. Therefore, when testing smaller RoM, the exponential increase in torque at the RoM limits may not be noticeable (Ragonesi et al., 2012). This non-linear behaviour is attributed to the muscle force-length relationship and the hard limits of joint structure (Wiegner and Watts, 1986; Maggioni et al., 2016).

The statistical analysis demonstrated no significant difference in PJI between the examined conditions, allowing us to choose a measure of convenience for identifying the elbow PJI and modelling it across the tested conditions. Considering the occasional elevated muscle activity observed in the 0.20 rad/s condition and the longer trial duration associated with slow velocities, we recommend a single dynamic trial at 0.10 rad/s in the neutral SFP for measuring and modelling the elbow PJI within the range of tested conditions. This condition offers a faster pace than static and

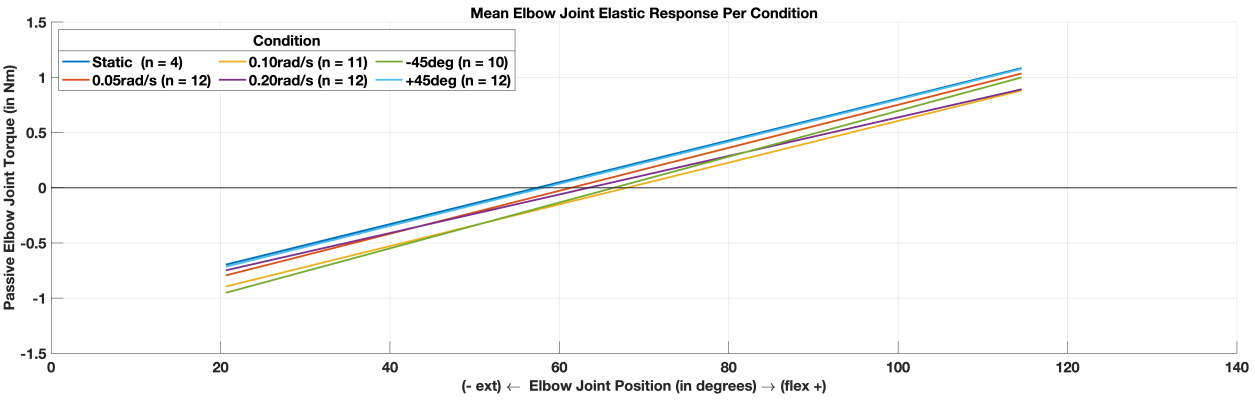


**Figure 8:** The Elastic Response regression models obtained by averaging all included trials under each condition.

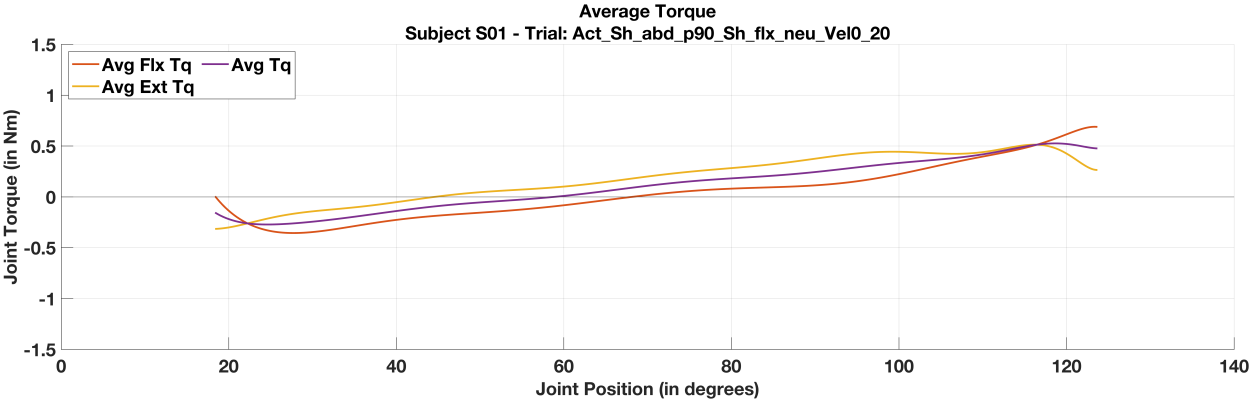


**Figure 9:** Dynamic trial 0.20 rad/s of S01 showing the hysteresis curves of flexion (red) and extension (yellow) crossing over each other due to increased muscle activity.

0.05 rad/s conditions without presenting the same muscle activity observed at 0.20 rad/s. Additionally, the neutral SFP avoids constraints posed by reduced pRoM.

To model the elbow PJI and generate a compensation signal for force-based controlled active assistive exoskeleton devices, we recommend utilising a regression model, which offers a generalised model that avoids overfitting the data, making it applicable to a broader population. An individual's elbow PJI model can be generated by obtaining a single dynamic measurement. The coefficients can be adjusted to accommodate potential changes occurring over time, such as thixotropy and temperature variations (Sekihara et al., 2007; Lakie et al., 1986), fatigue (Zhang and Rymer, 2001; Jones et al., 1987; Bottas et al., 2010; Pisano et al., 1996) or short-range stiffness (Drake and Charles, 2014; MacKay et al., 1986; de Vlugt et al., 2011).

Furthermore, existing literature has established a relationship between muscle cross-sectional area and changes in PJI (Durand et al., 2018), indicating a correlation between upper arm volume and elbow PJI (Wiegner and Watts, 1986). Our study also observed a linear correlation between the upper arm volume and the PJI of the dynamic condition of 0.10 rad/s at a neutral SFP.

Moreover, the influence of velocity warrants further investigation, especially for higher velocities (Kuxhaus et al., 2014; Wu et al., 2018). However, velocities beyond 30 and 60 deg/s (Wiegner and Watts, 1986; Pisano et al., 1996) may trigger a stretch reflex response, contributing to the observed PJI (MacKay et al., 1986; Sinkjær and Hayashi, 1989; Pisano et al., 1996; Lee et al., 2004; Bottas et al., 2010; Wang et al., 2017; Klomp et al., 2018; Wu et al., 2018). When testing higher velocities, we recommend replacing the applied triangular input position signal with a sinusoidal signal to mitigate the effects of inertia resulting from high accelerations at the change of movement direction (Pisano et al., 1996; Zhang et al., 2000; Sepehri et al., 2007).

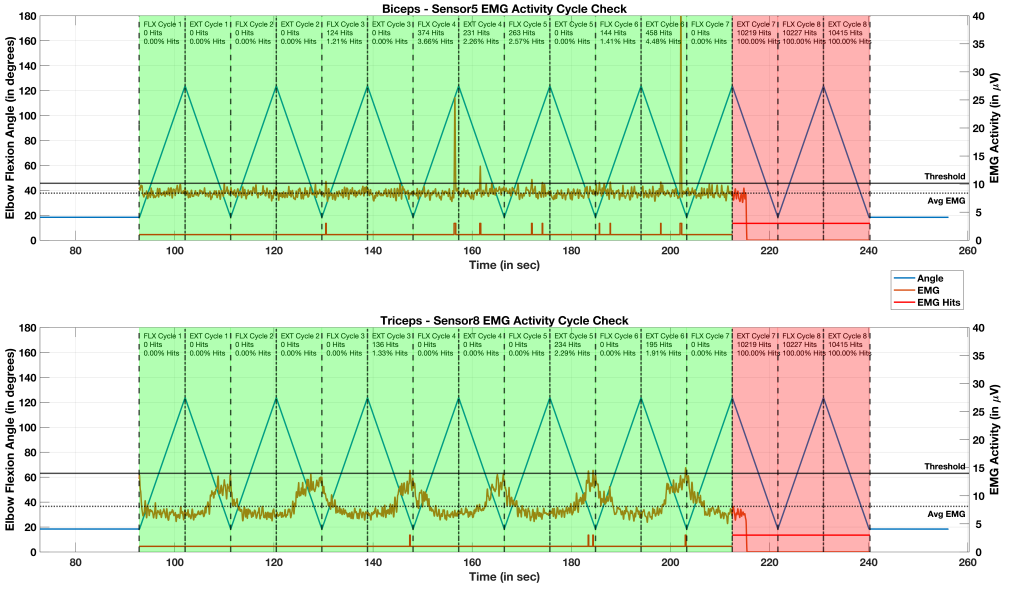


**Figure 10:** Selection of cycles based on the muscle activity of biceps brachii (top) and triceps brachii (bottom) of S01 condition $0.20\,\mathrm{rad/s}$. Synchronised elbow position from the actuator data (blue curve) and sEMG activity (orange curve) present the muscle activity during the trial. The included and excluded cycle phases are indicated in green and red, respectively. When more than $5\,\%$ of either of the two muscles' sEMG activity of a contraction phase surpasses the sEMG threshold (solid black line), the particular contraction phase is excluded. The red curve indicates the sEMG data samples which surpassed the threshold. The extension phase of cycle seven and the entire cycle eight are excluded due to flat sEMG. Due to the higher threshold, the rest of the cycles are not excluded despite the elevated muscle triceps brachii activity.

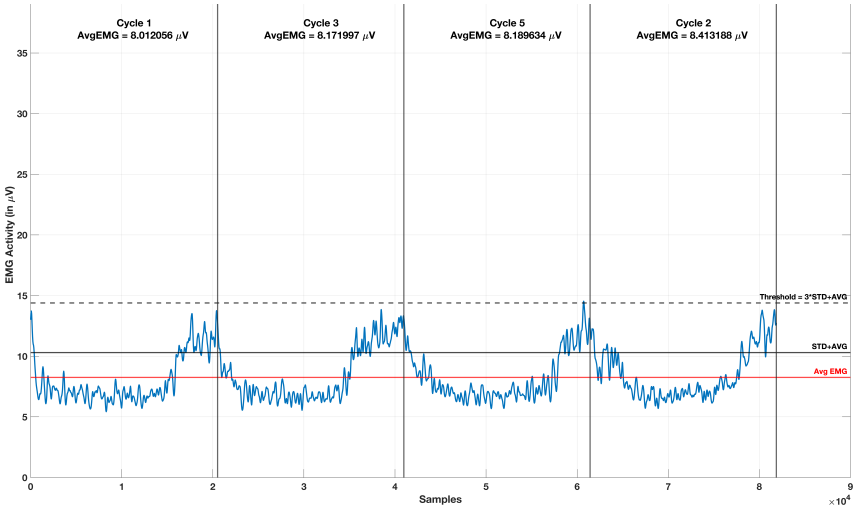


**Figure 11:** Four cycles with the lowest average sEMG activity of the triceps brachii muscle of S01 $0.20\,\mathrm{rad/s}$ dynamic trial. The three first cycles are used for the calculation of the noise and the threshold for excluding the cycles exhibiting increased muscle activity.

In our study, we deliberately focused on the 90° shoulder abduction position to eliminate the influence of gravity. However, exploring the effects of different shoulder abduction and flexion positions where the gravity component is present would be beneficial for future research. In these cases, precise mass measurements of the forearm would be essential to assess the individual contributions of gravity and PJI accurately. Limited shoulder flexion pRoM of two subjects indicates that investigating $-22°$ is more feasible than $-45°$.

Finally, it is worth noting that significant variations exist in pRoM and PJI measurements between healthy and non-healthy subjects (Sepehri et al., 2007; Ragonesi et al., 2012; Lobo-Prat et al., 2016; Wu et al., 2018). Therefore, it is imperative to conduct separate investigations and modelling of elbow PJI for non-healthy individuals to gain a comprehensive understanding of their unique biomechanical characteristics.

## 5. Conclusion

Individuals with neuromuscular diseases are greatly affected by elevated PJI, highlighting the importance of its accurate identification to detect user intention and improve the control of force-based active assistive devices. Despite their efforts, some subjects failed to maintain complete relaxation during measurements, which led to the exclusion of a substantial portion of the data. Regardless of the loss of data, we successfully modelled the elbow PJI for all tested conditions using a general regression model without overfitting the data. With statistical analysis revealing no significant differences in PJI under the conditions investigated, we conclude that a single condition is sufficient for measuring and modelling the elbow PJI. Consequently, we recommend using one experimental condition, specifically that of $0.10\,\mathrm{rad/s}$ in neutral SFP, due to its short duration and reduced muscle activity. Future research should explore higher velocities and different shoulder positions to uncover PJI differences. Finally, our findings stress the importance of investigating a tailored PJI model for non-healthy individuals when designing active assistive devices, considering observed variations in RoM and increased PJI with conditions like DMD.

## Acknowledgements

I would like to thank my supervisors, drs.ir Suzanne Filius and Prof.dr.ir Jaap Harlaar for their supervision and guidance during my thesis project and for offering me the opportunity to be part of this project and work with them. I would also like to thank my colleague Tom Wei with whom I worked on this project.

I must express my very profound gratitude to my parents, Constantinos and Chrystalla, who supported and encouraged me throughout this process and without whom this accomplishment would not have been possible. I would also like to thank my brother Stephanos and close friends for their support and encouragement, and lastly, my friend Konstantinos Tsifoutis-Kazolis, both as a friend and as the second reader of this thesis, for his support, advice and valuable comments. Dedicated to the memory of my grandmother Eleni.

## References

ATI, . FAQ - Force/Torque Sensors. ATI - Industrial Automation. URL: https://www.ati-ia.com/library/documents/FT_FAQ.pdf.

Boon, K., Hof, A., Wallinga-de Jonge, W., 1973. The mechanical behaviour of the passive arm, in: Biomechanics III. Karger Publishers. volume 8, pp. 243–248.

Bottas, R., Miettunen, K., Komi, P.V., Linnamo, V., 2010. Disturbed motor control of rhythmic movement at 2 h and delayed after maximal eccentric actions. Journal of Electromyography and Kinesiology 20, 608–618.

Brooke, M., Fenichel, G., Griggs, R., Mendell, J., Moxley, R., Florence, J., King, W., Pandya, S., Robison, J., Schierbecker, J., et al., 1989. Duchenne muscular dystrophy: patterns of clinical progression and effects of supportive therapy. Neurology 39, 475–475.

Clauser, C.E., Mc Conville, J.T., Young, J.W., 1969. Weight, volume, and center of mass of segments of the human body. Technical Report.

Cornu, C., Goubel, F., Fardeau, M., 2001. Muscle and joint elastic properties during elbow flexion in Duchenne muscular dystrophy. The Journal of Physiology 533, 605–616. URL: https://onlinelibrary.wiley.com/doi/full/10.1111/j.1469-7793.2001.0605a.xhttps://onlinelibrary.wiley.com/doi/abs/10.1111/j.1469-7793.2001.0605a.xhttps://physoc.onlinelibrary.wiley.com/doi/10.1111/j.1469-7793.2001.0605a.x, doi:10.1111/J.1469-7793.2001.0605A.X.

Dai, H., Otten, B., Mehrkens, J.H., D'Angelo, L.T., 2013. A portable system for quantitative assessment of parkinsonian rigidity, in: 2013 35th Annual International Conference of the IEEE Engineering in Medicine and Biology Society (EMBC), IEEE. pp. 6591–6594.

Demir, G., Bulut, N., Yılmaz, Ö., Karaduman, A., Alemdaroğlu-Gürbüz, İ., 2020. Manual ability and upper limb performance in nonambulatory stage of duchenne muscular dystrophy. Archives de Pédiatrie 27, 304–309.

Dempster, W., 1955. Space requirements of the seated operator. Technical Report.

Deshpande, A.D., Gialias, N., Matsuoka, Y., 2011. Contributions of intrinsic visco-elastic torques during planar index finger and wrist movements. IEEE Transactions on Biomedical Engineering 59, 586–594.

Drake, W.B., Charles, S.K., 2014. Passive stiffness of coupled wrist and forearm rotations. Annals of biomedical engineering 42, 1853–1866.

Durand, S., Rohan, C.P.Y., Hamilton, T., Skalli, W., Krebs, H.I., 2018. Passive wrist stiffness: the influence of handedness. IEEE Transactions on Biomedical Engineering 66, 656–665.

Gialias, N., Matsuoka, Y., 2006. A musculotendon contribution for multijoint hand control, in: 2006 International Conference of the IEEE Engineering in Medicine and Biology Society, IEEE. pp. 4482–4485.

Günzkofer, F., Engstler, F., Bubb, H., Bengler, K., 2011. Isometric elbow flexion and extension joint torque measurements considering biomechanical aspects, in: First International Symposium on Digital Human Modeling, pp. 14–15.

Harlaar, J., Becher, J., Snijders, C., Lankhorst, G., 2000. Passive stiffness characteristics of ankle plantar flexors in hemiplegia. Clinical Biomechanics 15, 261–270. URL: https://www.sciencedirect.com/science/article/pii/S0268003399000698, doi:https://doi.org/10.1016/S0268-0033(99)00069-8.

Hermens, H.J., Freriks, B., Merletti, R., Stegeman, D., Blok, J., Rau, G., Disselhorst-Klug, C., Hägg, G., 1999. European recommendations for surface electromyography. Roessingh research and development, Enschede, The Netherlands.

Holmes, M.W., Tat, J., Keir, P.J., 2015. Neuromechanical control of the forearm muscles during gripping with sudden flexion and extension wrist perturbations. Computer methods in biomechanics and biomedical engineering 18, 1826–1834.

Janssen, M.M., Bergsma, A., Geurts, A.C., De Groot, I.J., 2014. Patterns of decline in upper limb function of boys and men with dmd: an international survey. Journal of neurology 261, 1269–1288.

Janssen, M.M., Harlaar, J., Koopman, B., De Groot, I.J., 2017. Dynamic arm study: quantitative description of upper extremity function and activity of boys and men with duchenne muscular dystrophy. Journal of neuroengineering and rehabilitation 14, 1–14.

Jones, D., Newham, D., Clarkson, P., 1987. Skeletal muscle stiffness and pain following eccentric exercise of the elbow flexors. Pain 30, 233–242.

Klomp, A., De Groot, J.H., De Vlugt, E., Meskers, C.G., Arendzen, J.H., Van Der Helm, F.C., 2013. Perturbation amplitude affects linearly estimated neuromechanical wrist joint properties. IEEE Transactions on Biomedical Engineering 61, 1005–1014.

Klomp, A., de Vlugt, E., de Groot, J.H., Meskers, C.G., Arendzen, J.H., van der Helm, F.C., 2018. Perturbation velocity affects linearly estimated neuromechanical wrist joint properties. Journal of Biomechanics 74, 207–212.

Kuxhaus, L., Zeng, S., Robinson, C.J., 2014. Dependence of elbow joint stiffness measurements on speed, angle, and muscle contraction level. Journal of biomechanics 47, 1234–1237.

Lakie, M., Walsh, E., Wright, G., 1986. Control and postural thixotropy of the forearm muscles: changes caused by cold. Journal of Neurology, Neurosurgery & Psychiatry 49, 69–76.

Landin, D., Thompson, M., 2011. The shoulder extension function of the triceps brachii. Journal of Electromyography and Kinesiology 21, 161–165.

Lee, H.M., Chen, J.J.J., Ju, M.S., Lin, C.C.K., Poon, P.P., 2004. Validation of portable muscle tone measurement device for quantifying velocity-dependent properties in elbow spasticity. Journal of Electromyography and Kinesiology 14, 577–589.

Lin, C.C., Ju, M.S., Lin, C.W., 2003. The pendulum test for evaluating spasticity of the elbow joint. Archives of physical medicine and rehabilitation 84, 69–74.

Lobo-Prat, J., Keemink, A.Q., Koopman, B.F., Stienen, A.H., Veltink, P.H., 2015. Adaptive gravity and joint stiffness compensation methods for force-controlled arm supports, in: 2015 IEEE International Conference on Rehabilitation Robotics (ICORR), pp. 478–483. doi:10.1109/ICORR.2015.7281245.

Lobo-Prat, J., Kooren, P.N., Janssen, M.M., Keemink, A.Q., Veltink, P.H., Stienen, A.H., Koopman, B.F., 2016. Implementation of emg-and force-based control interfaces in active elbow supports for men with duchenne muscular dystrophy: A feasibility study. IEEE transactions on neural systems and rehabilitation engineering 24, 1179–1190.

Lobo-Prat, J., Nizamis, K., Janssen, M.M., Keemink, A.Q., Veltink, P.H., Koopman, B.F., Stienen, A.H., 2017. Comparison between semg and force as control interfaces to support planar arm movements in adults with duchenne: a feasibility study. Journal of neuroengineering and rehabilitation 14, 1–17.

MacKay, W., Crammond, D., Kwan, H., Murphy, J., 1986. Measurements of human forearm viscoelasticity. Journal of biomechanics 19, 231–238.

Maggioni, S., Melendez-Calderon, A., Van Asseldonk, E., Klamroth-Marganska, V., Lünenburger, L., Riener, R., Van Der Kooij, H., 2016. Robot-aided assessment of lower extremity functions: a review. Journal of neuroengineering and rehabilitation 13, 1–25.

Mayhew, A.G., Coratti, G., Mazzone, E.S., Klingels, K., James, M., Pane, M., Straub, V., Goemans, N., Mercuri, E., Group, P.W., et al., 2020. Performance of upper limb module for duchenne muscular dystrophy. Developmental Medicine & Child Neurology 62, 633–639.

McDonald, C.M., Abresch, R.T., Carter, G.T., Fowler, W.M., Johnson, E.R., Kilmer, D.D., Sigford, B.J., 1995. Profiles of neuromuscular diseases. duchenne muscular dystrophy. American journal of physical medicine & rehabilitation 74, S70–92. URL: https://pubmed-ncbi-nlm-nih-gov.tudelft.idm.oclc.org/7576424/, doi:10.1097/00002060-199509001-00003.

Mendell, J.R., Lloyd-Puryear, M., 2013. Report of mda muscle disease symposium on newborn screening for duchenne muscular dystrophy. Muscle & nerve 48, 21–26.

Mirbagheri, M.M., AliBiglou, L., Thajchayapong, M., Lilaonitkul, T., Rymer, W.Z., 2006. Comparison of neuromuscular abnormalities between upper and lower extremities in hemiparetic stroke, in: 2006 International Conference of the IEEE Engineering in Medicine and Biology Society, IEEE. pp. 303–306.

van den Noort, J.C., Bar-On, L., Aertbeliën, E., Bonikowski, M., Brændvik, S.M., Broström, E.W., Buizer, A.I., Burridge, J.H., van Campenhout, A., Dan, B., et al., 2017. European consensus on the concepts and measurement of the pathophysiological neuromuscular responses to passive muscle stretch. European journal of neurology 24, 981–e38.

Pando, A.L., Lee, H., Drake, W.B., Hogan, N., Charles, S.K., 2014. Position-dependent characterization of passive wrist stiffness. IEEE Transactions on Biomedical Engineering 61, 2235–2244.

Pandya, S., Florence, J.M., King, W.M., Robison, J.D., Oxman, M., Province, M.A., 1985. Reliability of goniometric measurements in patients with duchenne muscular dystrophy. Physical Therapy 65, 1339–1342.

Pisano, F., Miscio, G., Colombo, R., Pinelli, P., 1996. Quantitative evaluation of normal muscle tone. Journal of the neurological Sciences 135, 168–172.

Plagenhoef, S., Evans, F.G., Abdelnour, T., 1983. Anatomical data for analyzing human motion. Research quarterly for exercise and sport 54, 169–178.

Ragonesi, D., Agrawal, S., Sample, W., Rahman, T., 2011. Series elastic actuator control of a powered exoskeleton, in: 2011 Annual International Conference of the IEEE Engineering in Medicine and Biology Society, IEEE. pp. 3515–3518.

Ragonesi, D., Agrawal, S.K., Sample, W., Rahman, T., 2012. Quantifying anti-gravity torques for the design of a powered exoskeleton. IEEE Transactions on Neural Systems and Rehabilitation Engineering 21, 283–288.

Roberson, L., Giurintano, D.J., 1995. Objective measures of joint stiffness. Journal of Hand Therapy 8, 163–166.

Sekihara, C., Izumizaki, M., Yasuda, T., Nakajima, T., Atsumi, T., Homma, I., 2007. Effect of cooling on thixotropic position-sense error in human biceps muscle. Muscle & Nerve: Official Journal of the American Association of Electrodiagnostic Medicine 35, 781–787.

Sepehri, B., Esteki, A., Ebrahimi-Takamjani, E., Shahidi, G.A., Khamseh, F., Moinodin, M., 2007. Quantification of rigidity in Parkinson's disease. Annals of Biomedical Engineering 35, 2196–2203. URL: https://link.springer.com/article/10.1007/s10439-007-9379-6, doi:10.1007/S10439-007-9379-6/FIGURES/15.

Sinkjær, T., Hayashi, R., 1989. Regulation of wrist stiffness by the stretch reflex. Journal of biomechanics 22, 1133–1140.

Straathof, P.T., Lobo-Prat, J., Schilder, F., Kooren, P.N., Paalman, M.I., Stienen, A.H., Koopman, B.F., 2016. Design and control of the A-Arm: An active planar arm support for adults with Duchenne muscular dystrophy. Proceedings of the IEEE RAS and EMBS International Conference on Biomedical Robotics and Biomechatronics 2016-July, 1242–1247. doi:10.1109/BIOROB.2016.7523801.

de Vlugt, E., van Eesbeek, S., Baines, P., Hilte, J., Meskers, C.G., de Groot, J.H., 2011. Short range stiffness elastic limit depends on joint velocity. Journal of Biomechanics 44, 2106–2112. doi:10.1016/J.JBIOMECH.2011.05.022.

Wang, J.F., Forst, J., Schröder, S., Schröder, J.M., 1999. Correlation of muscle fiber type measurements with clinical and molecular genetic data in Duchenne muscular dystrophy. Neuromuscular Disorders 9, 150–158. doi:10.1016/S0960-8966(98)00114-X.

Wang, R., Herman, P., Ekeberg, Ö., Gäverth, J., Fagergren, A., Forssberg, H., 2017. Neural and non-neural related properties in the spastic wrist flexors: An optimization study. Medical Engineering & Physics 47, 198–209.

Wiegner, A.W., Watts, R.L., 1986. Elastic properties of muscles measured at the elbow in man: I. Normal controls. Journal of Neurology, Neurosurgery & Psychiatry 49, 1171–1176. URL: https://jnnp.bmj.com/content/49/10/1171https://jnnp.bmj.com/content/49/10/1171.abstract, doi:10.1136/JNNP.49.10.1171.

Winter, D.A., 2009. Biomechanics and motor control of human movement. John wiley & sons.

Winters, J.M., Kleweno, D.G., 1993. Effect of initial upper-limb alignment on muscle contributions to isometric strength curves. Journal of Biomechanics 26, 143–153.

Wu, Y.N., Park, H.S., Chen, J.J., Ren, Y., Roth, E.J., Zhang, L.Q., 2018. Position as well as velocity dependence of spasticity—four-dimensional characterizations of catch angle. Frontiers in Neurology 9, 863.

Zhang, L.Q., Park, H.S., Ren, Y., 2009. Shoulder, elbow and wrist stiffness in passive movement and their independent control in voluntary movement post stroke, in: 2009 IEEE International Conference on Rehabilitation Robotics, IEEE. pp. 805–811. doi:10.1109/ICORR.2009.5209489.

Zhang, L.Q., Portland, G.H., Wang, G., Diraimondo, C.A., Nuber, G.W., Bowen, M.K., Hendrix, R.W., 2000. Stiffness, viscosity, and upper-limb inertia about the glenohumeral abduction axis. Journal of Orthopaedic Research 18, 94–100. URL: https://onlinelibrary.wiley.com/doi/full/10.1002/jor.1100180114https://onlinelibrary.wiley.com/doi/abs/10.1002/jor.1100180114https://onlinelibrary.wiley.com/doi/10.1002/jor.1100180114, doi:10.1002/JOR.1100180114.

Zhang, L.Q., Rymer, W.Z., 2001. Reflex and Intrinsic Changes Induced by Fatigue of Human Elbow Extensor Muscles. Journal of Neurophysiology 86, 1086–1094. URL: https://www.physiology.org/doi/10.1152/jn.2001.86.3.1086, doi:10.1152/jn.2001.86.3.1086.

**Table 7**
Quick overview of FT sensor technical data.

| Range of Measurement | | | Resolution | | |
|---|---|---|---|---|---|
| $F_x, F_y$ (±N) | $F_z$ (±N) | $M_x, M_y, M_z$ (±Nm) | $F_x, F_y$ (N) | $F_z$ (N) | $M_x, M_y, M_z$ (Nm) |
| 80 | 240 | 4 | 0.02 | 0.04 | 0.001 |

**Table 8**
Quick overview of FT sensor Euler angles and translations to align its coordinate system to the forearm and express it at the elbow joint centre.

| Euler Angles | | | Translations | | |
|---|---|---|---|---|---|
| $\phi_x$ | $\phi_y$ [a] | $\phi_z$ | $TransX$ | $TransY$ | $TransZ$ |
| −1.5° | ≈ 5° | 17.9° | −138.82 mm | 63.5 mm | 55 mm |

[a] Calibrated every time before and after each trial to compensate for changes in the shoulder flexion angle.

# A. Appendix I: Force Sensor

## A.1. Overview

For the measurement of the interaction forces between the user and the elbow device, we use a six-axis force/torque (FT) sensor FT-Mini-40 SI-80-4 (Schunk GmbH & Co. KG, Germany) measuring through strain gauges the strain applied in all six degrees-of-freedom (DOF) ($F_x$, $F_y$, $F_z$, $M_x$, $M_y$, $M_z$). Fig. 12 shows the coordinate system as provided by the manufacturer and in Fig. 1, how the FT sensor is positioned on the setup.

To measure the Elbow Joint Torque (EJT), we must express the forces and torques measured from the location of the FT sensor to the setup's elbow joint centre (EJC). With the joint flexed at 90° and relative to the EJC, the FT sensor is positioned +138.82 mm distally, +55 mm superiorly to the forearm (or to the EJC when the elbow is flexed at 90°) and +63.5 mm medially (see Fig. 1). Every time, a series of steps is applied to the measurements, beginning with the conversion of the raw signals, bias offset, rotation and finally, translation of all six components. Following an initial calibration for identifying the bias values and the Euler angles, there still needs to be a daily calibration measurement to compensate for any other changes that may arise. Table 8 gives an overview of the FT sensor coordinate system Euler angles and translations. All the custom written *Matlab* functions are stored in a private repository.

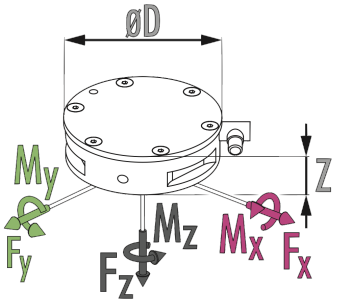


**Figure 12**
FT sensor FTD-Mini-40 SI-80-4 (Schunk GmbH & Co. KG, Germany) coordinate system as provided by manufacturer's product information.

## A.2. Signal Conversion

The FT sensor signals or Gage Outputs are recorded in a signed 16-bit integer number ranging from -32768 to 32767 ($Gage_{out}$). These values need to be converted to voltages using the following equation:

$$V_{out} = V_{max} * \frac{Gage_{out}}{counts} = 10 * \frac{Gage_{out}}{counts}, \tag{1}$$

where $V_{out}$ the measured forces and torques measured in the ±10 V analogue voltage range, $V_{max} = 10$ V, the maximum voltage range for the recorded signals and $counts = 2^{16}/2$ (unitless). Then, the signals are converted to forces [N] and torques [Nm] through the matrix multiplication of the $V_{out}$ with the [6x6] calibration matrix, which the manufacturer provides.

## A.3. Bias Values Identification

The FT measurement needs to be zeroed or biased before each experiment. We made an extensive calibration before the study and during the trials, we did a simpler and faster calibration process before and after each participant's session. To avoid output drift, we carried out each calibration at least 50 min (30 to 45 min per the manufacturer's suggestion) after powering on the system, giving ample time for the sensor to warm up, its temperature to equalise and the outputs to stabilise. The biasing of each sample of the FT measurements is achieved through the following:

$$FT_{\text{biased}} = \begin{bmatrix} F_x \\ F_y \\ F_z \\ M_x \\ M_y \\ M_z \end{bmatrix}_{\text{biased}} = \begin{bmatrix} F_x \\ F_y \\ F_z \\ M_x \\ M_y \\ M_z \end{bmatrix}_{\text{raw}} - \begin{bmatrix} bias F_x \\ bias F_y \\ bias F_z \\ bias M_x \\ bias M_y \\ bias M_z \end{bmatrix} \tag{2}$$

### *A.3.1. Before trials*

Before the trials, we performed an initial calibration by detaching the FT sensor from the setup and positioning it in three different directions to obtain the mean force and torque values over a 15 s window. To calibrate FT sensor signals we used the custom *matlab* function `fun_identifyCalibrationValues.m`. The calibration steps are:

1. Z-Axis facing the ground, where we calibrate $F_x$, $F_y$ and $M_z$,
2. X-Axis facing upwards to calibrate $F_z$ and $M_x$ and finally,
3. Y-Axis facing upwards for the calibration of $M_y$

### *A.3.2. During Trials*

Due to the time required to carry out the bias experiment with the detached FT sensor, during the trials, we performed a different process which takes less time and can be repeated regularly throughout the day, before and after each participant's experimental session. In this process, the actuator is moving through an extended RoM from $-70°$ to $275°$ at $0.1\,\text{rad/s}$ for one full flexion/extension cycle, while a 1.5 kg mass (approximately the total mass of hand and forearm) is attached to the setup's sleeve, right under the centre of the FT sensor (see Fig.14c). We fit a 6th-order polynomial to each FT sensor signal (*Matlab* function `polyfit`) and calculate their corresponding bias difference as the average between the peak and valley of each curve. Through the following equation, we updated the bias value by adding the difference to the existing ones:

$$bias_{i_{\text{new}}} = bias_{i_{\text{old}}} + \frac{\max(signal_i) + \min(signal_i)}{2}, \tag{3}$$

where $signal_i$ can be any of the six FT sensor signals. For this calibration process, we used the custom *matlab* function `fun_checkCalibrationValuesOnline.m`. An example is displayed in Fig.13. During the trials, we also corrected for changes in the Euler angle about the $Y$-axis. For more information on the process, refer to subsection A.4.2.

## A.4. Euler-Angle Identification

To properly read the interaction forces and torques applied by the user, we aligned the FT sensor coordinate system to the forearm through a series of rotations (see Fig. 1). To identify the three Euler angles, we used two static and one dynamic trial while attaching a mass to the system. For the static experiments, we used two different constant elbow positions to derive the Euler angles about the $X$- and $Z$-axes, and with the dynamic trial where the elbow joint moved through the RoM of $-70°$ to $275°$, we derived the $Y$-axis Euler angle. In all static cases, the shoulder joint remained in the $0°$ flexion and abduction position. Because of the setup design where the active DoF moves in the $X$-$Z$ plane, the $Y$-axis Euler angle was the only one derived from a dynamic investigation. In contrast, we calculated the other two Euler angles at constant positions. We used a spirit level to position the shoulder and elbow joints to ensure the correct setup position. For the static trials, we used the spirit level to direct the $X$- and $Z$-axes to face directly down, i.e. $\theta_{\text{elbow}} = 0°$ and $\theta_{\text{elbow}} = 90°$, respectively. We estimated the Euler angles in the $ZYX$ order by updating the rotation matrix with each newly identified Euler angle each time. The process was repeated until all Euler angles converged to 1 decimal point. For these experiments, we utilised a mass-holder for attaching additional masses to the system (see Fig. 14b).

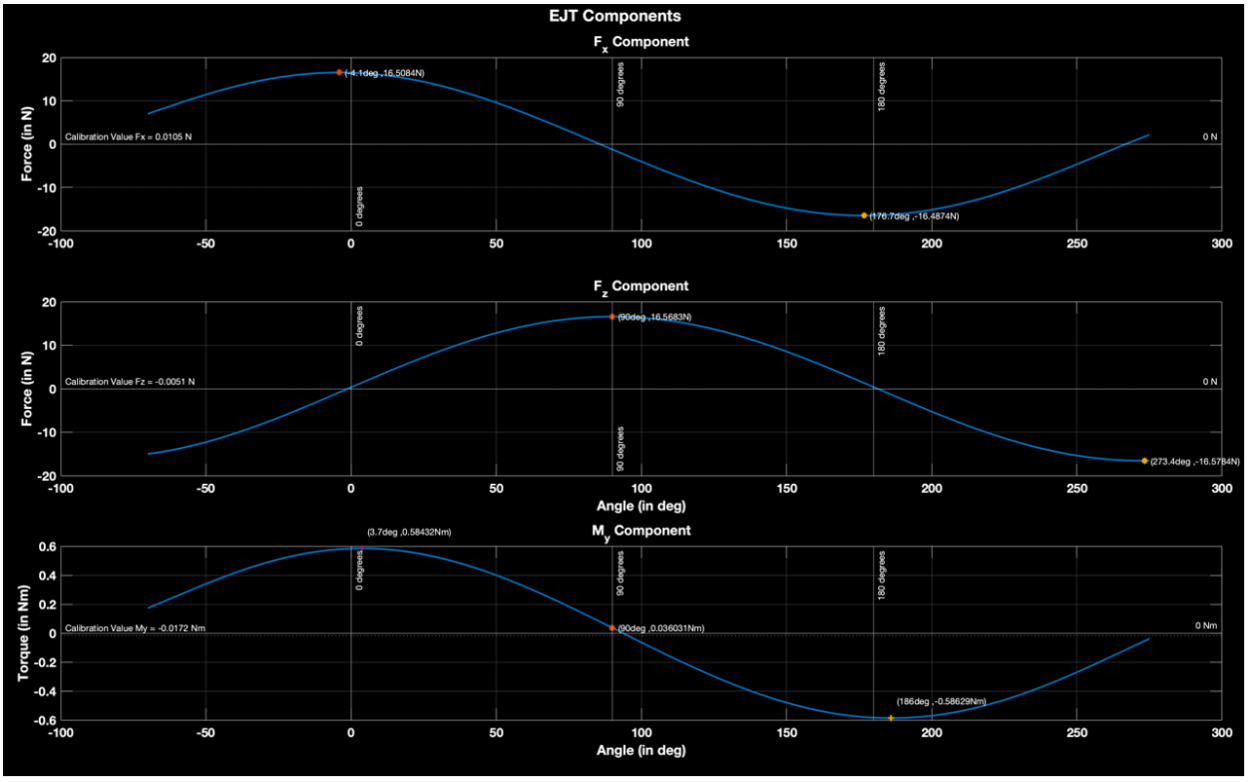


**Figure 13:** Bias calibration of $F_x$, $F_z$ and $M_y$ during the trials. Based on the average value between the peak and valley of the signals, we calculate the bias correction. To adjust the Euler angle about the $Y$-axis ($\phi_y$), we align the $F_z$ peak to the 90° elbow joint position.

### *A.4.1. Static Experiments*

The two positions of the static investigations involved the measurement of the weight in only the $F_x$ and $F_z$ components and respectively deriving the Euler angles about the $Z$- and $X$-axes by minimising all other force components. For the static experiments, the arm of the device was positioned and remained in a single position. At the same time, we consecutively added 500 g-masses to increase the total attached mass to 1500 g before removing them one by one in the reverse order. A 30-second window intermediated each mass addition/removal, allowing ample time for the system to reach and remain in equilibrium to obtain an average force measurement. The total mass attached to the system during each step was 0 g, 500 g, 1000 g, 1500 g, 1000 g, 500 g and 0 g (with a COM approximately positioned right under the centre of the FT sensor). An additional 175 g for the mass-holder is added to each case.

After manually selecting the windows with the most stable readings (out of each 30 s-window recording), we create new force signals from the concatenated windows. To obtain the Euler angles, we apply rotations in steps of 0.1° until, based on the cost function, the $F_x$ or $F_z$ components are maximised, and the other components are minimised. More information on the cost functions is available in section A.5.

*Pure $F_x$ → Derive Rot-$Z$* To derive the $Z$-Axis Euler angle, the device arm was positioned at a shoulder abduction and flexion of 0° and a fully extended elbow joint (i.e. $\theta_{\text{elbow}} = 0°$), resulting in a theoretically positive pure $F_x$ measurement of the weight. For the $Z$-axis Euler angle, the $F_y$ component was minimised. We identified the Euler angle $\phi_Z = 17.9°$, which we confirmed by manually measuring the rotation of the force sensor with a goniometer and deriving the angle to be approximately 18°. An example of the process is presented in Fig. 15.

*Pure $F_z$ → Derive Rot-$X$* To derive the $X$-Axis Euler angle, the elbow joint was flexed at 90°, resulting in a theoretically positive pure $F_z$ weight measurement. Similarly to before, we minimised the cost of the $F_y$ component and we derived the Euler angle to be $\phi_x = -1.5°$.

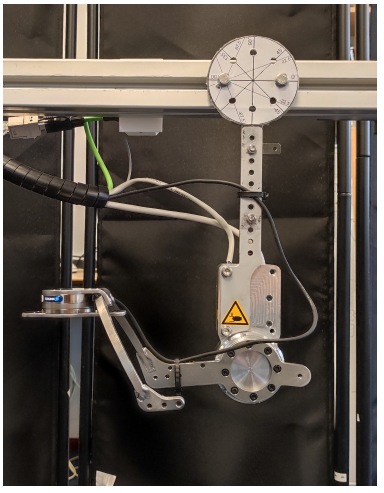

**(a)** FT sensor with only the force plate attached.

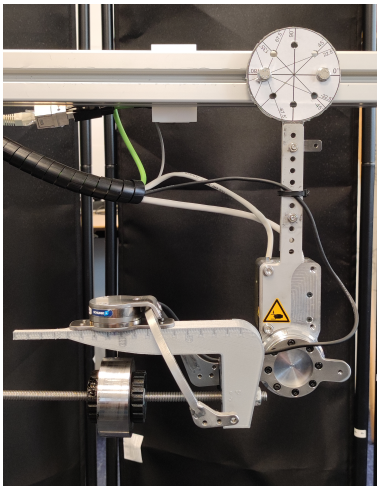

**(b)** FT sensor with the mass-holder and a 500 g-mass attached.

**(c)** FT sensor with the sleeve and a mass attached inside the sleeve.

**Figure 14:** Mass-holder (14b) and sleeve attachments (14c) used for the calibration of the FT sensor during the trials.

### *A.4.2. Dynamic Experiment*

To obtain the Euler angle about the $Y$-axis, we utilised an elbow dynamic motion of one complete flexion/extension cycle through $-70°$ to $275°$ and back, at a constant velocity of $0.1\,\mathrm{rad/s}$, while having a $1.5\,\mathrm{kg}$ mass attached to the system. We used the mass holder for the initial FT sensor calibration, whereas, during the experimental trials with the subjects, we attached the mass to the sleeve. We decided to keep the sleeve attached to the system during the subject trials and avoid disassembling parts of the setup to prevent any potential calibration issues. We identify the peak of the $F_z$ force component to determine the Euler angle about the $Y$-axis. If it does not occur at $90°$ elbow joint angle, we apply rotation steps of $0.1°$ until the $F_z$ peak occurs at $90°$ (see Fig. 13). We chose the $F_z$ component for identifying the Euler angle because of its greater contribution to the EJT due to its higher moment arm.

The elbow joint is the only active joint with a sensor to measure its position relative to the upper arm. The orientation of the upper arm changes with the shoulder joint position and as a result, the Euler angle $\phi_y$, is susceptible to changes in the shoulder flexion position. These changes can either be the result of testing different shoulder flexion positions, where we manually adjust it during the trials, or when adjusting the setup height. For this reason, $\phi_y$ is the only Euler angle we calibrated during the trials. The approximate value is $\phi_y \approx 5°$. For a summary of rotation and translation values, refer to Table 8.

### *A.4.3. Rotation Matrix*

Once we obtain all the Euler angles, the rotations can be applied all together with the following:

$$R = \left(R_x * R_y * R_z\right)^{-1} = R_z^{-1} * R_y^{-1} * R_x^{-1},$$

$$R = \begin{bmatrix} c_y * c_z & -c_y * s_z & s_y \\ c_x * s_z + c_z * s_x * s_y & c_x * c_z - s_x * s_y * s_z & -c_y * s_x \\ s_x * s_z - c_x * c_z * s_y & c_z * s_x + c_x * s_y * s_z & c_x * c_y \end{bmatrix}^{-1}, \text{ where} \tag{4}$$

$$R_x = \begin{bmatrix} 1 & 0 & 0 \\ 0 & \cos(\phi_x) & -\sin(\phi_x) \\ 0 & \sin(\phi_x) & \cos(\phi_x) \end{bmatrix} \quad R_y = \begin{bmatrix} \cos(\phi_y) & 0 & \sin(\phi_y) \\ 0 & 1 & 0 \\ -\sin(\phi_y) & 0 & \cos(\phi_y) \end{bmatrix} \quad R_z = \begin{bmatrix} \cos(\phi_z) & -\sin(\phi_z) & 0 \\ \sin(\phi_z) & \cos(\phi_z) & 0 \\ 0 & 0 & 1 \end{bmatrix}$$

$c$ and $s$ are the short form for the cos() and sin() functions, and $x, y, z$ the short form for the Euler angles $\phi_x, \phi_y$ and $\phi_z$. Finally, the rotation matrix with which we premultiply the FT sensor signals is expressed by:

$$\text{Rotation Matrix} = \begin{bmatrix} R & 0 \\ 0 & R \end{bmatrix}, \text{a } 6 \times 6 \text{ matrix} \tag{5}$$

## A.5. Euler Angle Cost Functions

During each rotation step, the angle is assessed using a cost function, and the angle corresponding to the lowest cost is chosen as the Euler angle for the rotation of the coordinate system of the FT sensor. Overall, we have tested three different cost functions and selected the one using the "equal mean" criterion as the most suitable. The three cost functions we have evaluated include (1) equal mean (EM), (2) smallest two (ST), and (3) full (full). An overview of the Euler angle each one of these cost functions gives for a particular example is available in Fig. 15. This process is done by the custom *Matlab* function `fun_minimiseCostFunction.m`.

For a particular force component, we calculate the absolute average force over each window (i.e. rectangles in Fig. 15) with the following equation:

$$F_{\text{window}} = \left| \frac{\sum_{i=1}^{N} F_i}{N} \right|, \tag{6}$$

where $N$ is the number of samples in a single window.

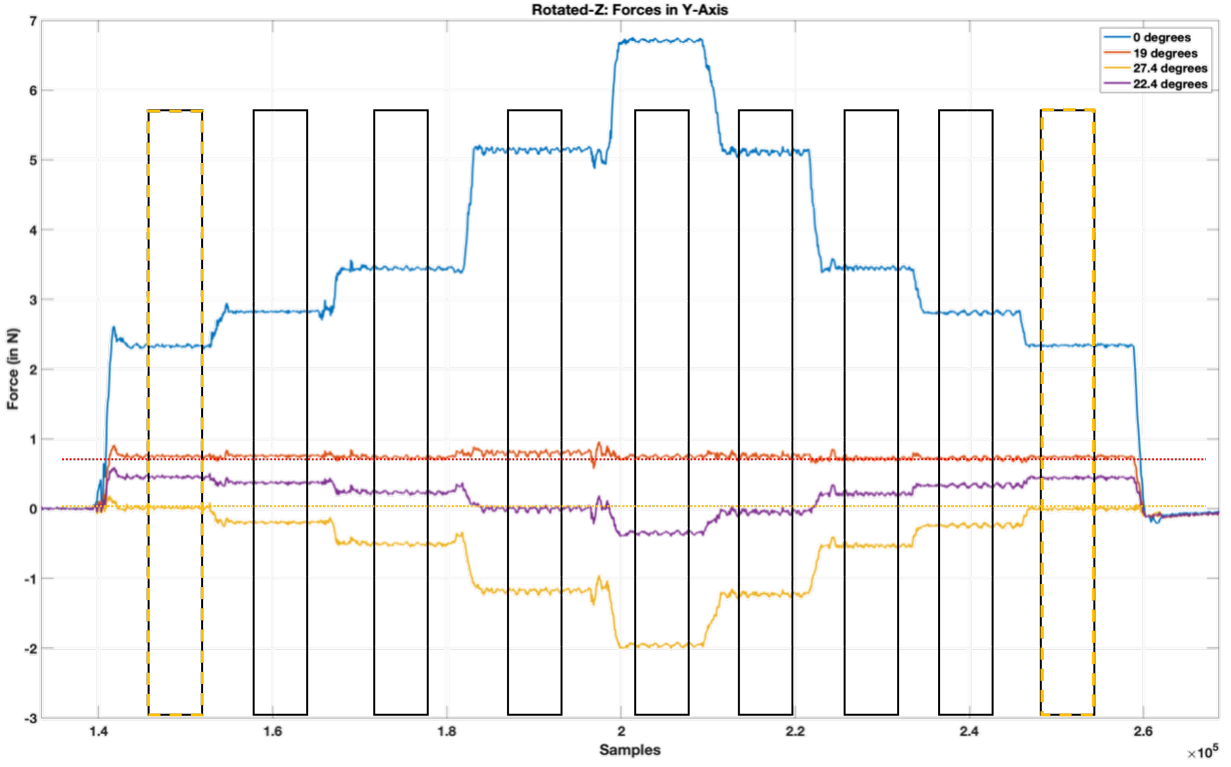


**Figure 15:** Example of the process of minimising the cost functions on the original (blue curve) $F_y$ component by applying rotations about the $Z$-axis. Rectangles represent individual windows with different masses. The Euler angle estimated by each cost function is displayed in the legend, with the rotated $F_y$ signal based on these Euler angles displayed in red, orange and purple for the "equal mean", "smallest two" and "full" respectively. All black rectangles are used for the "equal mean" and "full" cost functions, whereas the orange dashed rectangles are used only for the "smallest two" cost function. The red dotted line indicates the absolute average force over all the non-zero mass windows $F_{\text{EM}}$ around which the "equal mean" cost function operates. On the other hand, the orange dotted line represents the 0 N line around which the "smallest two" and "full" cost functions estimate their cost. This example includes more steps of added mass instead of 500 g.

### *A.5.1. Equal Mean*

This cost function calculates the cost ($cost_{\text{EM}}$) as the total difference between all the non-zero mass windows (excludes 1st and last window with no added weight) and the absolute average force over all the non-zero mass windows $F_{\text{EM}}$, using the following equations:

$$F_{\text{EM}} = \left| \frac{\sum_{j=1}^{L} F_{\text{window}_j}}{L} \right|, \tag{7}$$

$$cost_{\text{EM}} = \sum_{j=1}^{L} \left| F_{\text{window}_j} - F_{\text{EM}} \right|, \tag{8}$$

where $j$ and $L$, are the index and the total number of non-zero mass windows, respectively. The result is a “straight" line throughout the trial, where additional mass does not seem to affect the force component (see red curve in Fig. 15).

### *A.5.2. Smallest two*

In this case, the cost ($cost_{\text{SM}}$) is derived based on the two non-zero mass windows with the smallest added mass. Finds the smallest total difference of the two windows from 0 N with the equation:

$$cost_{\text{SM}} = \sum_{j=1}^{K} F_{window_j}, \tag{9}$$

where $j$ is the index of the non-zero mass window and $K = 2$ is the total number of non-zero mass windows with the smallest mass. The result is optimizing for the 2nd and 2nd to last windows, which have the two smallest added masses so that the absolute average force in these two windows is as close to zero as possible (see the orange curve in Fig. 15).

### *A.5.3. Full*

Similarly to EM, the 3rd cost function calculates the cost ($cost_{\text{full}}$) based on all the non-zero mass windows, however, it minimises the difference from the 0 N instead of the absolute average force over all the non-zero mass windows. The equation used is:

$$cost_{\text{full}} = \sum_{j=1}^{L} F_{window_j}, \tag{10}$$

where $j$ and $L$ are the index of non-zero mass windows and the total number of all the non-zero mass windows, respectively. In Fig. 15, the result is represented by the purple curve.

## A.6. Elbow Joint Torque Estimation

Following the rotation of the FT sensor coordinate system to align it with the forearm as was described in the previous section, measuring the EJT requires also the translation of the FT sensor coordinate system to the setup’s EJC (see Fig. 1).

### *A.6.1. Translations*

The translations of all three axes are derived from the 3D model of the setup and we express them in a matrix form as shown below:

$$T = \begin{bmatrix} 0 & TransZ & -TransY \\ -TransZ & 0 & TransX \\ TransY & -TransX & 0 \end{bmatrix}$$

$$TranslationMatrix = \begin{bmatrix} I & 0 \\ T & I \end{bmatrix}, \text{a } 6 \times 6 \text{ matrix}, \tag{11}$$

where $I$ the identity matrix, and $TransX$, $TransY$ and $TransZ$ the translation values from Table 8.

#### *A.6.2. Transformed Output Measurements*

To align the FT coordinate system to the forearm and express it at the setup's EJC (eq. 13), we premultiply the biased FT output signals (eq. 2) with the Transformed Matrix (eq. 12). The Transformed Matrix (eq. 12) results from the product of the Rotation Matrix (eq. 5) and Translation Matrix (eq. 11), with the rotations being applied first and the translations second. The transformed output FT measurements are filtered with a 2nd-order Low-Pass Butterworth filter with a cut-off frequency of 10 Hz. The EJT is expressed by the $M_y$ component of eq. 13. Following the rotation of the FT sensor coordinate system, the EJT is calculated by $EJT = M_y - (F_x * TransZ) + (F_z * TransX)$.

$$\text{TransformedMatrix} = \text{TranslationMatrix} \times \text{RotationMatrix} \tag{12}$$

$$FT_{\text{Transformed}} = \text{TransformedMatrix} \times FT_{\text{biased}} \tag{13}$$

### A.7. Validation of Force Sensor Elbow Joint Torque

During the trials, as instructed by the manufacturer in the FT sensor FAQ manual (ATI), we calibrated the FT sensor before each experiment. In total, we did three calibrations per day, one before and one after each experiment (two experiments per day). The calibration process included a dynamic experiment, as described in subsection "During Trials" in section A.4.2, where we calculated the new bias values (see Fig. 13) along with a new Euler angle for the $Y$-axis (see Fig. 13) to compensate for any reading changes and setup adjustments.

Furthermore, we validated the EJT reading against a provided gravity model of the arm. Based on the assumption that the gravity model is correct, we calibrated the FT sensor while using the sleeve and adjusting the signals to match the gravity model as best as possible. During the validation process, we adjusted the translation in the $Z$-axis ($TransZ$) to match the EJT peak with the 90° elbow joint position (see Fig. 16). The accuracy of the EJT was ensured with an RMS error less than 0.1 Nm. For the validation, we used the custom *Matlab* function `fun_estmatedEJT_Validation.m`.

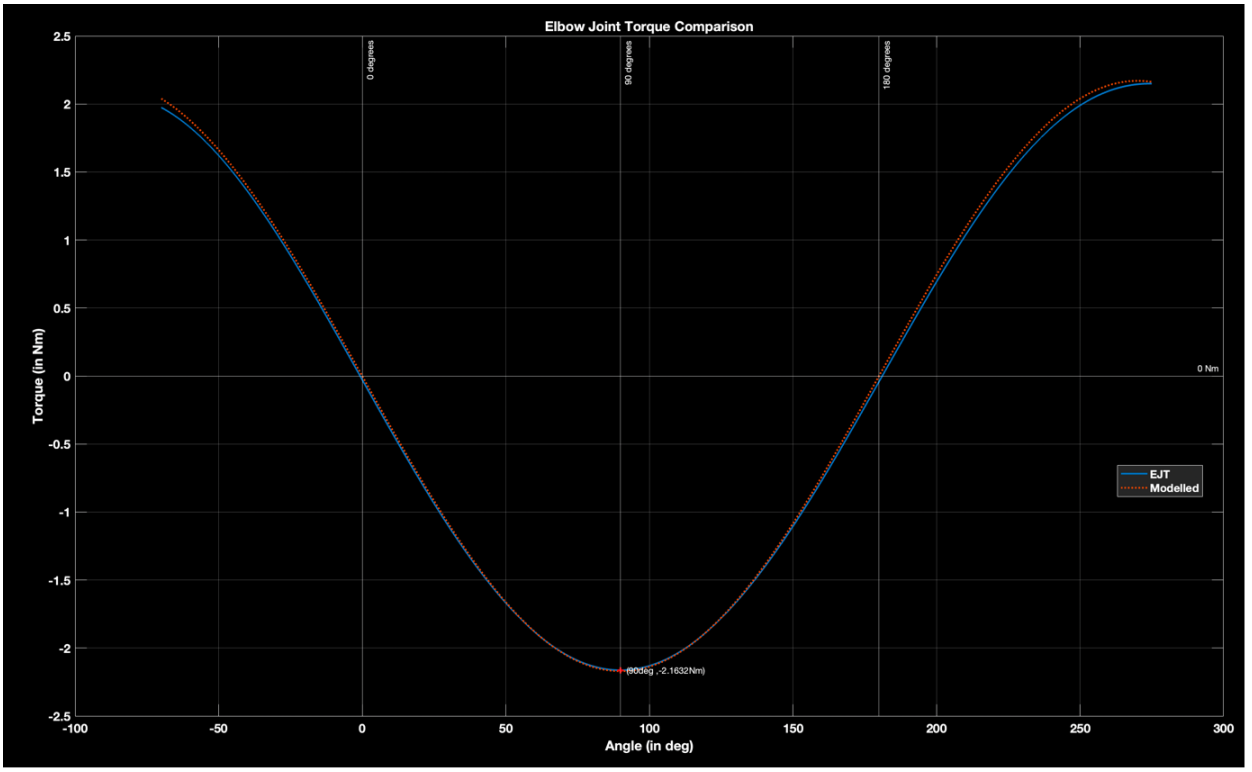


**Figure 16:** Validation of the EJT against the arm gravity model before an experimental session, with the use of an 1.5 kg.

# B. Appendix II: Electromyography

To prepare the skin of the user, we shaved any excess hair and cleaned it with alcohol. We attached the sensors to the skin with adhesive tape. For the experiments, visual inspection of the surface EMG (sEMG) activity during and at the end of each experiment ensured the correct recording of the data. On some occasions, even though during the experiment the live sEMG displayed no abnormalities or signal interruption between the base and the wireless sensors; the post-trial visual inspection of the sEMG signal showed missing parts. In this case, we repeated the experiment to obtain the complete sEMG recording.

## B.1. Muscle selection

In our study, we monitored the Biceps Brachii muscle (m. BB) and the Triceps Brachii muscle (m. TB). We also considered monitoring other muscles like the deltoid and brachioradialis, however, the actuator and the sleeve location were covering the sEMG electrode attachment points or would touch them during movement. Also, m. BB and m. TB are the primary muscles of elbow joint flexion and extension and provide the most activity related to these movements.

## B.2. EMG Exclusion

### *B.2.1. Static Trials*

For the static trials, the baseline muscle activity is established through nine out of 23 (ratio 3:8) of the plateaus with the smallest average sEMG activity. For each trial, the sEMG signal of each muscle is treated separately. For a muscle, the average sEMG activity of each plateau ($\overline{\text{sEMG}}_{m,p}$) is calculated (see eq. 14) and then the plateaus are sorted in ascending order based on their average sEMG activity. Then, we select the first nine plateaus with the smallest activity. A new temporary signal is constructed from these nine plateaus (see eq. 15 and Fig. 17), out of which the baseline electrical activity ($\text{sEMG}_{\text{baseline}_m}$) of the muscle for the particular trial is calculated as the average (see eq. 16) and the noise is estimated as the standard deviation (SD) (see eq. 17). Finally, the threshold indicating activity in the muscle is calculated as three times the noise over the average sEMG activity (see eq. 18).

$$\overline{\text{sEMG}}_{m,p} = \frac{\sum_{k=1}^{N} \text{sEMG}_{m,p}(k)}{N}, \tag{14}$$

$$\text{sEMG}_{\text{relaxed}_m} = \begin{bmatrix} \text{sEMG}_{m,q_1} & \text{sEMG}_{m,q_2} & \cdots & \text{sEMG}_{m,q_Q} \end{bmatrix}, \text{where } \text{sEMG}_{m,q_1} < \text{sEMG}_{m,q_2} < \cdots < \text{sEMG}_{m,q_Q} \tag{15}$$

$$\text{sEMG}_{\text{baseline}_m} = \frac{\sum_{q=1}^{Q} \overline{\text{sEMG}}_{m,q}}{Q}, \tag{16}$$

$$\text{noise}_m = \text{SD}(\text{sEMG}_{\text{relaxed}_m}) \tag{17}$$

$$\text{threshold}_m = \text{sEMG}_{\text{baseline}_m} + (3 \cdot \text{noise}_m) \tag{18}$$

where $m$ is either m. BB or m. TB, $p$ is the plateau index, $N$ is the number of sEMG samples in the plateau, $k$ is the data sample index, $\text{sEMG}_{m,q_i}$ is the sEMG activity of the plateau $i$ out of nine plateaus with the smallest sEMG activity, $q$ is the plateau index of the nine plateaus with the least average sEMG activity and $Q$ is nine, the number of relaxed plateaus.

Finally, for each trial, the inclusion of each plateau is evaluated based on the activity of both muscles. For each muscle, the average sEMG activity of each plateau ($\overline{\text{sEMG}}_{m,p}$) is compared to the sEMG threshold of the muscle ($\text{threshold}_m$). If the average sEMG plateau activity of either muscle surpasses their corresponding thresholds (i.e. $\overline{\text{sEMG}}_{m,p} > \text{threshold}_m$), then the plateau is excluded. An example of the included and excluded plateaus based on the sEMG activity is displayed in Fig. 18.

This process is based on the assumption that the average sEMG of a plateau indicates whether a subject is relaxed, and in these nine selected plateaus, the subject is relaxed, allowing us to extract a relaxed baseline activity threshold.

### *B.2.2. Dynamic Trials*

Similarly, for the dynamic trials, we separate each flexion/extension cycle sEMG activity and compare it to its corresponding threshold. Since dynamic trials have eight cycles, we use the same ratio (3:8) as in the static trials,

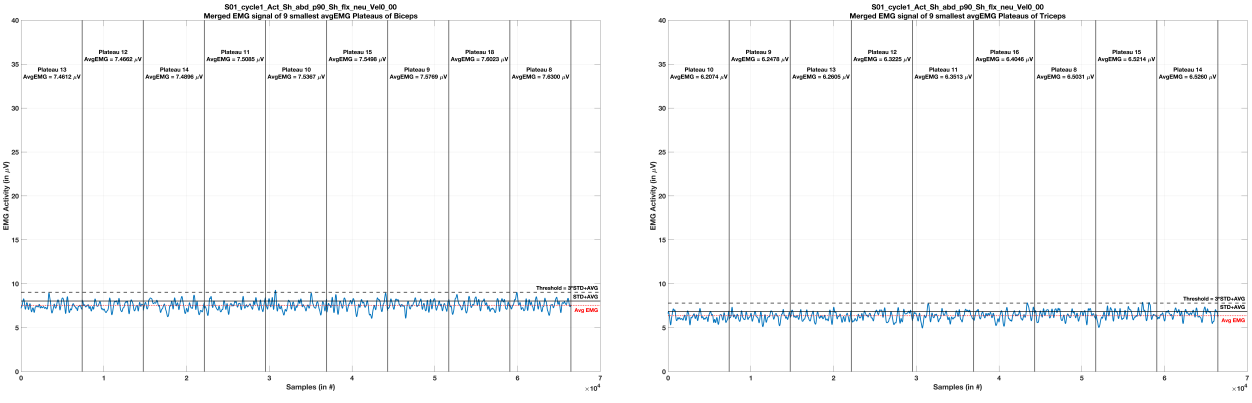


**(a)** The relaxed sEMG signal of m. BB.

**(b)** The relaxed sEMG signal of m. TB.

**Figure 17:** The relaxed sEMG signals of m. BB and m. TB of the static trial of S01, constructed from the first nine plateaus with the lowest average sEMG activity (eq. 15). Their corresponding relaxed baseline value is indicated by the red dotted line and the threshold with the black dashed line.

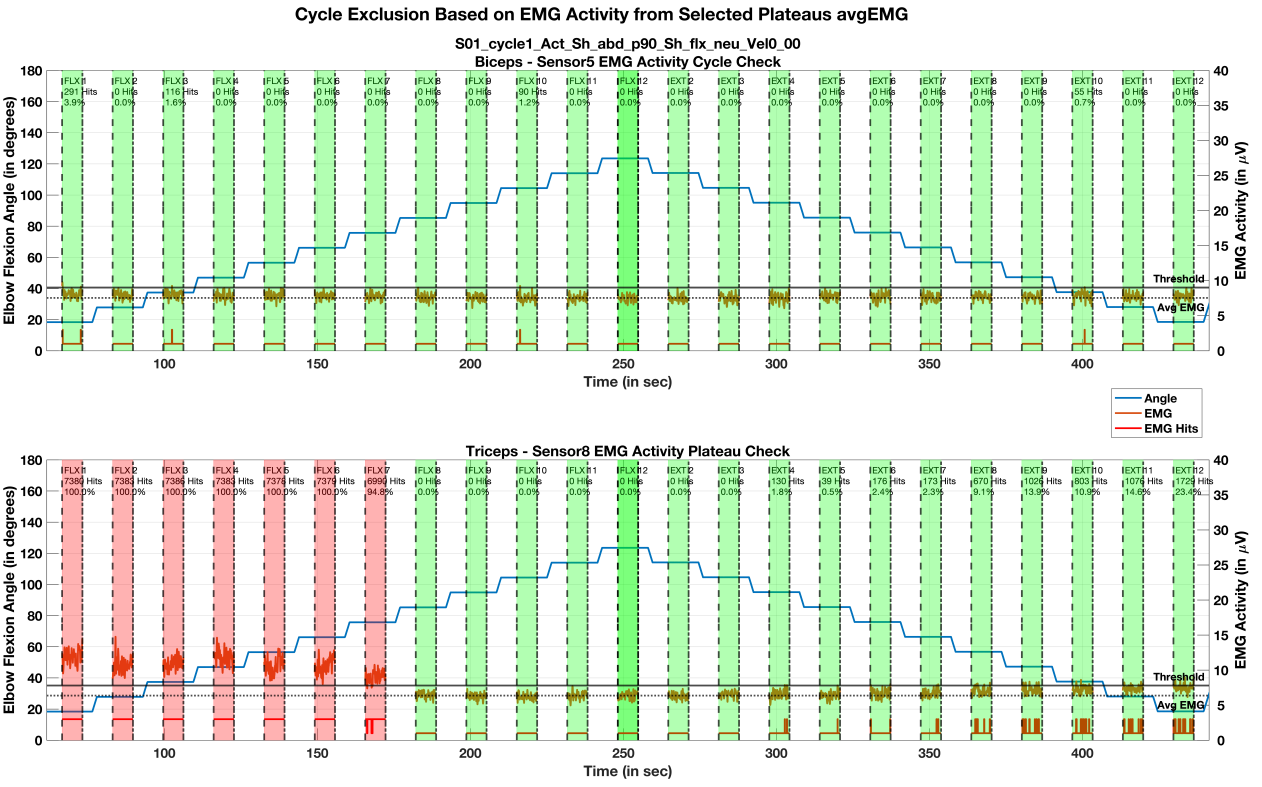


**Figure 18:** Example of subject 1 static experiment, where the EMG activity of the m. BB is on the top plot and of the m. TB at the bottom. The blue solid line indicates the elbow joint position during the trial and in orange, the EMG activity of the muscles. The calculated relaxed baseline value is indicated by the dotted line and the threshold with the solid black line. The red line at the bottom of each plot, indicates which data samples of each plateau surpass the threshold. Their percentage is indicated at the top of each plateau. The included plateaus are highligted in green and those of which the average EMG surpasses the threshold are excluded and highlighted in red.

assuming that in three of the eight recorded cycles (including 1st and last), the subject is relaxed. For each muscle, we calculate the average sEMG activity of every cycle (see eq. 14, where $p$ is the cycle index), and we place them all in ascending order. Then, a new temporary relaxed sEMG signal is constructed from the three cycles (instead of nine plateaus as in the static trial) with the lowest average sEMG activity (see eq. 15, where instead of nine plateaus we use three cycles, $Q = 3$) (see Fig. 11). Again, a relaxed baseline value is obtained by averaging the three most relaxed sEMG cycles (see eq. 16) and the noise is calculated by the standard deviation (see eq. 17). The activity threshold of each muscle is again calculated in the same way (see eq. 18). Upon estimating the threshold, to avoid any potential effects from the reflex response (MacKay et al., 1986; Klomp et al., 2018; Wu et al., 2018), short-range stiffness (MacKay et al., 1986; de Vlugt et al., 2011; Drake and Charles, 2014) or the subjects anticipating the onset or end of the movement (Holmes et al., 2015), we always excluded the first and last cycles from any further processing. We evaluate each cycle's flexion and extension phase separately, where each data sample is compared against the threshold ($\text{sEMG}_{m,p}(k) > \text{threshold}_m$) and if a minimum of 5 % of the contraction phase data samples surpass the threshold, then the contraction phase is excluded from further analysis. An example of the included and excluded cycles based on the sEMG activity is displayed in Fig. 10.

# C. Appendix III: Supplementary Figures and Tables

**Table 9**
Overview of included trials. Green colour is for included trials, and red for excluded.

| | | Velocity (rad $s^{-1}$) | | | Shoulder Flexion | | |
|---|---|---|---|---|---|---|---|
| Subject | Static | 0.05 | 0.10 | 0.20 | −45° | +45° | Total |
| 1 | | | | | | | 5 |
| 2 | | | | | | | 5 |
| 3 | | | | | | | 4 |
| 4 | | | | | | | 4 |
| 5 | | | | | | | 5 |
| 6 | | | | | | | 5 |
| 7 | | | | | | | 6 |
| 8 | | | | | | | 6 |
| 9 | | | | | | | 6 |
| 10 | | | | | | | 5 |
| 11 | | | | | | | 6 |
| 12 | | | | | | | 4 |
| Total | 4 | 12 | 11 | 12 | 10 | 12 | **61** |

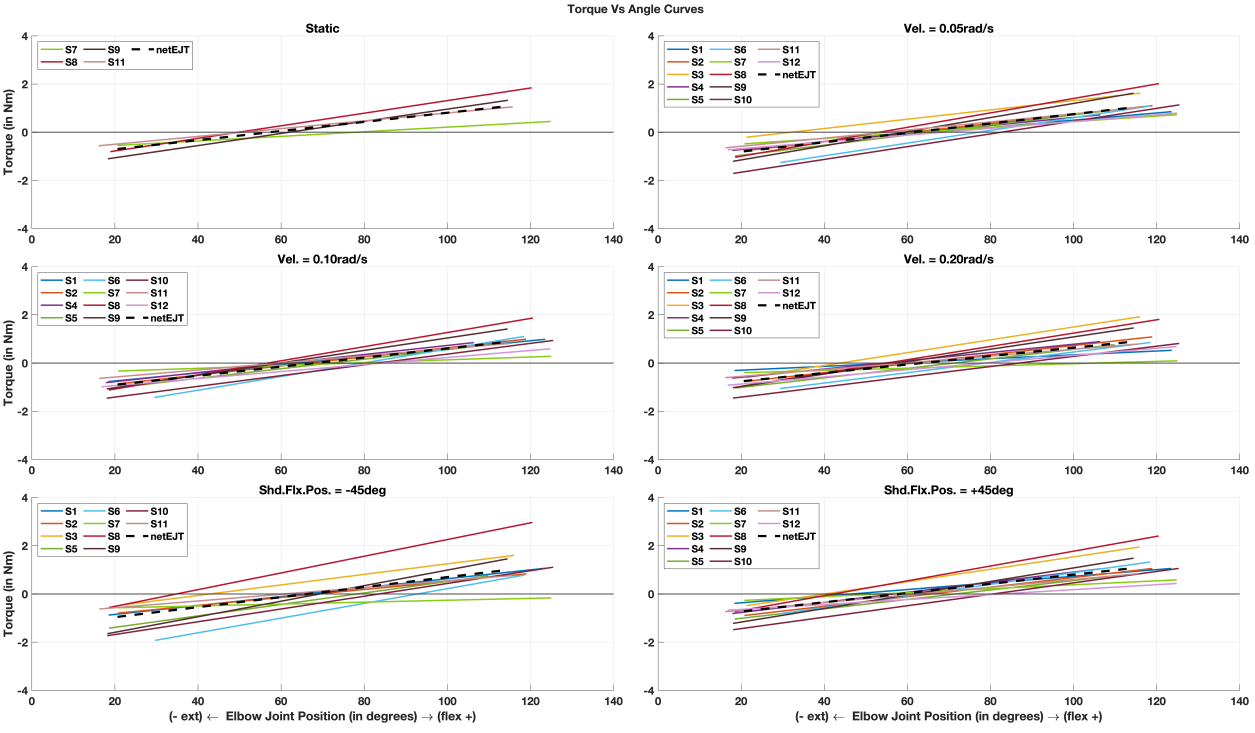


**Figure 19:** Elastic Response regression models of each included trial, classified into the different tested conditions. The black dashed line indicates the regression model obtained by averaging the $\overline{\text{EJT}}$ of the included trials in the common RoM of all the subjects.

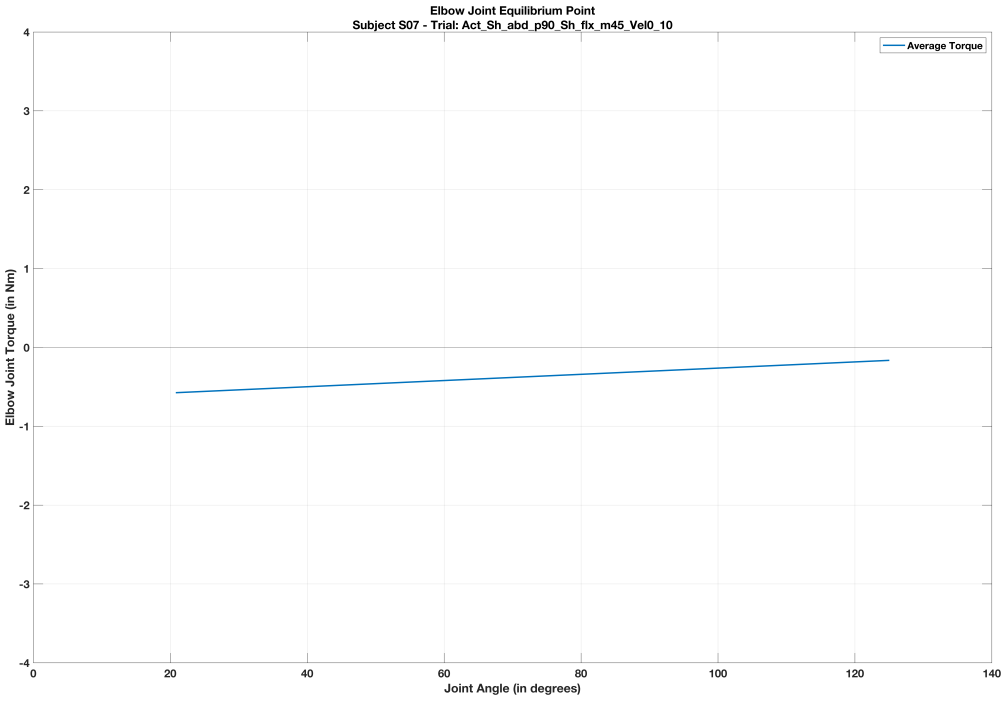


**Figure 20:** $\overline{EJT}$ regression model of S07 tested at −45° shoulder flexion position having only negative values, failing to obtain the EP.

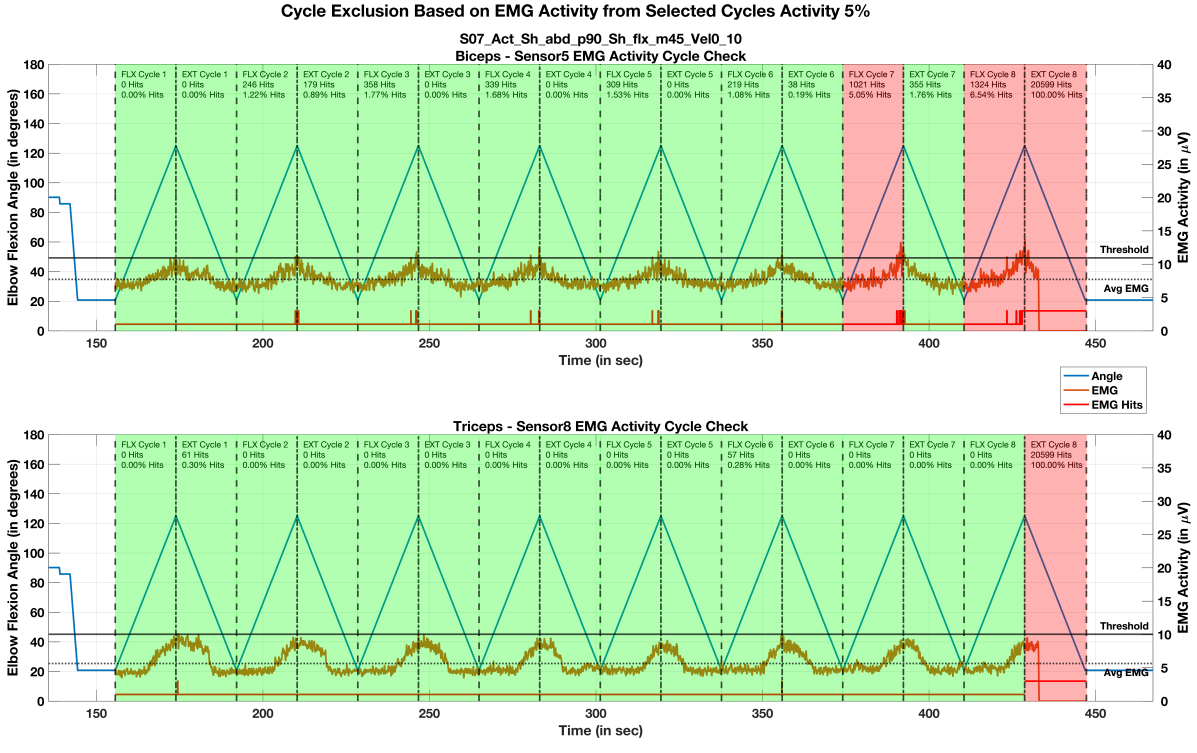


**Figure 21:** Trial of S07 at −45° shoulder flexion position, where we could not identify an equilibrium position because the elastic response never crossed the 0 Nm. We observe elevated sEMG activity in both muscles, especially around the most flexed position. Due to the activity present in all cycles, the noise is higher and so is the relaxed-state threshold. As a result, the exclusion process failed to eliminate the trial.

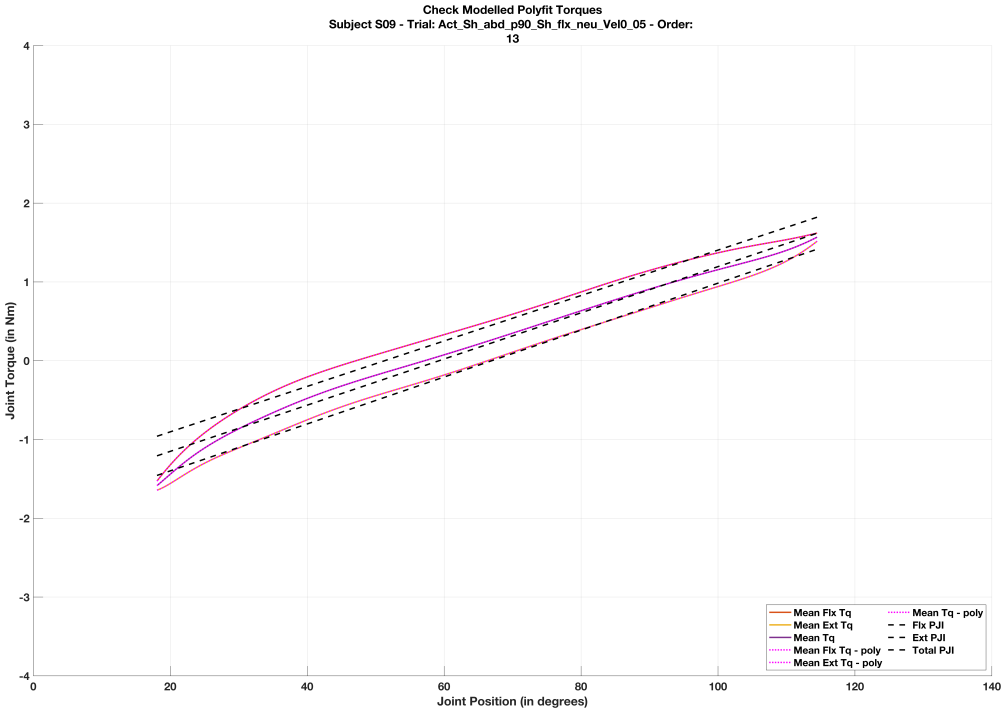


**Figure 22:** Example of fitting a regression model to the elastic response, as well as the net flexion and extension torques.